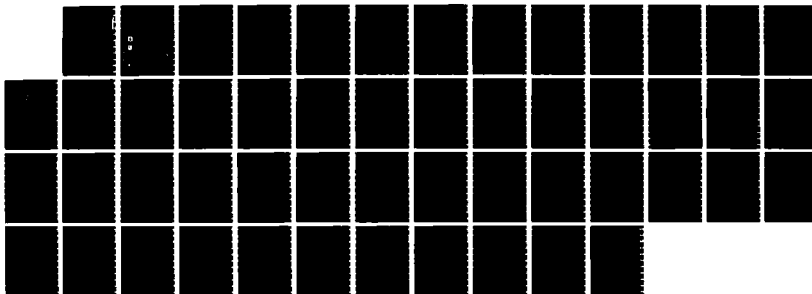
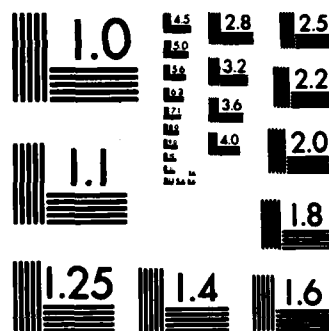


AD-A172 178 SPACE RADIATION DOSIMETER SSJ* FOR THE BLOCK 50/FLIGHT 1/1
7 DMSP (DEFENSE ME. (U) AIR FORCE GEOPHYSICS LAB
HANSCOM AFB MA H S GUSSENHOVEN ET AL. 28 MAR 86
UNCLASSIFIED AFGL-TR-86-0065 F/G 4/1 NL





AFGL-TR-86-0065
ENVIRONMENTAL RESEARCH PAPERS, NO. 949

AD-A172 178

Space Radiation Dosimeter SSJ * for the Block 5D/Flight 7 DMSP Satellite: Calibration and Data Presentation

M.S. GUSSENHOVEN
R.C. FILZ
K.A. LYNCH

E.G. MULLEN
F.A. HANSER



20 March 1986



Approved for public release; distribution unlimited.



DTIC
ELECTE
SEP 23 1986
E



SPACE PHYSICS DIVISION

PROJECT 7601


AIR FORCE GEOPHYSICS LABORATORY

HANSCOM AFB, MA 01731


DTIC FILE COPY

"This technical report has been reviewed and is approved for publication"

FOR THE COMMANDER



GARY MULLEN, Chief
Space Particles Environment Br
Space Physics Division



Rita C. Sagalyn, Director
Space Physics Division

This report has been reviewed by the ESD Public Affairs Office (PA) and is releasable to the National Technical Information Services (NTIS).

Qualified requestors may obtain additional copies from the Defense Technical Information Center. All others should apply to the National Technical Information Service.

If your address has changed, or if you wish to be removed from the mailing list, or if the addressee is no longer employed by your organization, please notify AFGL/DAA, Hanscom AFB, MA 01731. This will assist us in maintaining a current mailing list.

Unclassified

SECURITY CLASSIFICATION OF THIS PAGE

REPORT DOCUMENTATION PAGE

AD-A172178

1a. REPORT SECURITY CLASSIFICATION Unclassified			1b. RESTRICTIVE MARKINGS		
2a. SECURITY CLASSIFICATION AUTHORITY			3. DISTRIBUTION/AVAILABILITY OF REPORT Approved for public release; distribution unlimited.		
2b. DECLASSIFICATION/DOWNGRADING SCHEDULE					
4. PERFORMING ORGANIZATION REPORT NUMBER(S) AFGL-TR-86-0065 ERP, No. 949			5. MONITORING ORGANIZATION REPORT NUMBER(S)		
6a. NAME OF PERFORMING ORGANIZATION Air Force Geophysics Laboratory		6b. OFFICE SYMBOL (If applicable) PHP	7a. NAME OF MONITORING ORGANIZATION		
6c. ADDRESS (City, State and ZIP Code) Hanscom AFB Massachusetts 01731			7b. ADDRESS (City, State and ZIP Code)		
8a. NAME OF FUNDING/SPONSORING ORGANIZATION		8b. OFFICE SYMBOL (If applicable)	9. PROCUREMENT INSTRUMENT IDENTIFICATION NUMBER		
8c. ADDRESS (City, State and ZIP Code)			10. SOURCE OF FUNDING NOS.		
			PROGRAM ELEMENT NO. 62101F	PROJECT NO. 7601	TASK NO. 760120
			WORK UNIT NO. 76012002		
11. TITLE (Include Security Classification) Space Radiation Dosimeter SSJ* for the Block 5D/Flight 7 DMSP Satellite: (Contd)					
12. PERSONAL AUTHOR(S) M. S. Gussenhoven, R. C. Filz, K. A. Lynch, E. G. Mullen and F. A. Hanser*					
13a. TYPE OF REPORT Scientific. Interim.		13b. TIME COVERED FROM _____ TO _____		14. DATE OF REPORT (Yr., Mo., Day) 1986 March 20	
				15. PAGE COUNT 50	
16. SUPPLEMENTARY NOTATION *Panametrics Inc., Waltham, Massachusetts					
17. COSATI CODES			18. SUBJECT TERMS (Continue on reverse if necessary and identify by block number)		
FIELD	GROUP	SUB. GR.	Radiation		
			Dose		
			DMSP satellite		
			Relativistic protons		
			Relativistic electrons		
19. ABSTRACT (Continue on reverse if necessary and identify by block number) The DMSP/F7 satellite carries, in addition to weather monitoring devices, a number of instruments that measure the space environment for the purpose of scientific study. These are an auroral imaging device, precipitating electron and ion detectors, a thermal plasma analyzer, a fluxgate magnetometer, and a space radiation dosimeter. Together, these provide a strong tool for analyzing the high latitude, near-Earth, magnetospheric environment. This report has been prepared to facilitate the use of the data from one of these instruments, the space radiation dosimeter, and to show how the data can be used to obtain both dose and flux measurements of high energy electrons and protons at low altitudes. The report includes: a description of the DMSP/F7 orbit; a description of the space radiation dosimeter and the data it returns; the method by which dose is determined; the method by which flux is determined; and a discussion of the use of high threshold energy proton and ion induced star counts. In Appendices A and B we present the (Contd)					
20. DISTRIBUTION/AVAILABILITY OF ABSTRACT UNCLASSIFIED/UNLIMITED <input checked="" type="checkbox"/> SAME AS RPT. <input type="checkbox"/> DTIC USERS <input type="checkbox"/>			21. ABSTRACT SECURITY CLASSIFICATION Unclassified		
22a. NAME OF RESPONSIBLE INDIVIDUAL M. S. Gussenhoven			22b. TELEPHONE NUMBER (Include Area Code) (617) 377-3212		22c. OFFICE SYMBOL PHP

11. (Contd)

Calibration and Data Presentation

19. (Contd)

response of the dosimeter to electron bremsstrahlung and a list of the interactive routines available at AFGL for data analysis.

Contents

1. INTRODUCTION	1
2. THE DMSP/F7 ORBIT	3
3. THE DMSP/F7 DOSIMETER	3
4. CALCULATION OF THE DOSE SPECTRA	7
5. CALCULATION OF THE RESPONSE FUNCTION FOR PROTON FLUX SPECTRA	11
6. ELECTRON RESPONSE FUNCTIONS FROM CALIBRATION DATA	28
7. THE STAR COUNTS	34
REFERENCES	35
APPENDIX A: Dosimeter Response to Electron Bremsstrahlung	37
APPENDIX B: The J* Interactive Program, JSINTAP	41

ALITY
ECTED
1

iii

Accession For	
NTIS GRA&I	<input checked="" type="checkbox"/>
DTIC TAB	<input type="checkbox"/>
Unannounced	<input type="checkbox"/>
Justification	
By _____	
Distribution/	
Availability Codes	
Dist	Avail and/or Special
A-1	

Illustrations

1. Diurnal Orbital Coverage for North and South Poles Plotted in Corrected Geomagnetic Latitude (MLAT) and Magnetic Local Time (MLT)	4
2. Satellite Path Across the Band of Geographic Latitudes From 50° to -50°	5
3. Schematic of One of the Four Sensors	6
4. Survey Plot of Delta Dose Counts for the First Full Orbit on 3 February 1985	10
5. Depth Dose Spectra for Passage Through the Heart of the SAA on 3 February 1985 From 4355 to 5735 UT	11
6. Survey Plot of Flux Counts for the First Full Orbit on 3 February 1985	12
7. Limits of Integration for the Energy Dependent Geometric Factor for Protons	16
8. Response Function for a 400 μ Silicon Detector to a Flat Proton Spectrum Which is Isotropic and Has Unit Flux, for Incident Energies Between 1 to 1000 MeV and for Energy Deposition of 1 to 10 MeV (first curve), and Response Functions to the Same Spectrum for the Detector Behind Domes 1, 2, 3 and 4	17
9a. Energy Independent Geometric Factors for Protons as a Function of the Power Spectral Index for the HILET Flux Channels	21
9b. Energy Dependent Geometric Factors for Protons as a Function of the Power Spectral Index for the HILET Dose Channels	21
10a. Survey Plots for the J* Dosimeter for 16 February 1984 Showing Flux Counts	22
10b. Survey Plots for the J* Dosimeter for 16 February 1984 Showing Dose Counts	23
11. Relative Response Function for Protons of an Unshielded 400 μ Silicon Detector for the Trapped Mirror Plane Distribution at Different Values of the Magnetic Field Inclination	25
12. The Response Function of a 400 μ Silicon Detector to a Flat Proton Spectrum Which Has a Trapped Mirror Plane Distribution at a Magnetic Inclination Angle of 40°, for Incident Energies Between 1 to 1000 MeV and for Energy Deposition of 1 to 10 MeV (first curve), and Response Functions to the Same Spectrum for the Detector Behind Domes 1, 2, 3, and 4	27
13. Energy Dependent Geometric Factors as a Function of Energy for Electrons in the LOLET Channels	32
14. Angular Response to Electrons for the Dome 2 LOLET Channel	33

Tables

1. Design Parameters of Dome Sensors	7
2. Channel Dose Calibration Constants	8
3. Internal vs External Proton Energy for Different Domes	18
4a. Omnidirectional Geometric Factors of the Flux Channels for Protons in $\text{cm}^2 \text{ MeV}$	19
4b. Omnidirectional Geometric Factors of the Dose Channels for Protons in $\text{cm}^2 \text{ MeV}$	20
5. Average Count Rates (c/s) on 16 February 1984 From 35,596 to 35,656 UT	24
6. J(20): Count Rate $G(N)$ in $\text{P}/(\text{cm}^2 \text{ s MeV})$ From 35,596 to 35,656 UT on 16 February 1984	24
7. Response Function of 400 μ Bare Silicon Detector to a Delta Function Trapped Mirror Plane Distribution in the Infinite Slab Approximation (HILET Dose Channel) (Normalized by π -Area)	26
8. Omnidirectional Geometric Factors for the Trapped Mirror Plane Geometry for HILET Flux (PF) and Dose (PD) Channels in $\text{cm}^2 \text{ MeV}$	29
A1. LOLET Channel Responses to Electron Bremsstrahlung	40

Space Radiation Dosimeter SSJ* for the Block 5D/Flight 7 DMSP Satellite: Calibration & Data Presentation

1. INTRODUCTION

The Defense Meteorological Satellite Program (DMSP) of the U.S. Air Force is an operational program calling for two satellites to be in polar orbit at all times: one in the dawn-dusk meridian and one in the 1030 to 2230 LT meridian. The program is principally devoted to weather monitoring, but because of the satellite's excellent coverage of the auroral regions, it also supports a complement of special sensors (SS) designed for study of auroral dynamics. These include the SSJ/4 auroral electron and ion detectors (Hardy et al¹), the SSIE and SSIES thermal plasma experiments (Smiddy et al²), the SSM magnetometer (Rich et al³), and an X-ray imager. In addition, radiometers operating over the polar caps in darkness produce

(Received for publication 19 March 1986)

1. Hardy, D. A., Schmitt, L. K., Gussenhoven, M. S., Marshall, F. J., Yeh, H. -C., Schumaker, T. L., Huber, A., and Pantazis, J. (1984) Precipitating Electron and Ion Detectors (SSJ/4) for the Block 5D/Flights 6-10 DMSP Satellites: Calibration and Data Presentation, AFGL-TR-84-0317, AD A157080, Air Force Geophysics Laboratory, Hanscom AFB, Massachusetts.
2. Smiddy, M., Sagalyn, R. C., Sullivan, W. P., Wildman, P. J. L., Anderson, P., and Rich, F. (1978) The Topside Ionosphere Plasma Monitor (SSIE) for the Block 5D/Flight 2 DMSP Satellite, AFGL-TR-78-0071, AD A058503.
3. Rich, F. J. (1984) Fluxgate Magnetometer (SSM) for the Defense Meteorological Satellite Program (DMSP) Block 5D/2, Flight 7, AFGL-TR-84-0225, AD A155229, Air Force Geophysics Laboratory, Hanscom AFB, Massachusetts.

the now familiar auroral images. The DMSP/F7 satellite also carries a space radiation dosimeter which measures the flux of relativistic electrons and protons and the dose deposited by these particles behind four different thicknesses of aluminum shielding.

Auroral particle precipitation can create ionospheric disturbances that impede ground to spacecraft (aircraft) communication and detection. It can also be intense enough to cause spacecraft surface charging to several hundred volts (Gussenhoven et al⁴). Particles with sufficient fluxes to create these hazards have energies less than 100 keV. Relativistic particles (in the MeV range), despite their low fluxes, can also create a harsh environment for the operation of spacecraft in low altitude orbits. These particles can deposit sufficient energy in sensitive volumes, such as microelectronic devices or biological cells, to degrade or even destroy their performance ability. The critical energy deposition can be accumulated over substantial time periods from many particles (dose), or result from the passage of a single particle through a sensitive volume (single event upset). In the latter case the energy deposited may be from the incident particle alone or the incident particle may initiate a nuclear reaction in which the products also contribute to the energy deposited (star events).

There are two main sources for MeV particles at low altitudes: the more or less steady radiation belts, and the highly time dependent solar flare (or solar cosmic ray) particles. In addition, there is a steady background of galactic cosmic rays modulated by the 11-year cycle of solar activity. The radiation belt particles reach low altitudes in two regions. Outer zone electrons, whose flux varies over several orders of magnitude, map into a high latitude ring below the auroral zone. Radiation belt protons reach low altitudes in the South Atlantic Anomaly (SAA), a wide region centered near 30° S and 345° E, in geographic latitude and longitude, respectively. Solar cosmic rays, ejected during solar flares, are guided by solar magnetic field lines to the near-Earth region. Here they directly access the Earth's magnetic field lines above a minimum latitude. The DMSP orbits traverse all three regions of relativistic particle precipitation. The space radiation dosimeter was designed for the DMSP orbit to measure dose, dose rate, particle flux, and nuclear star events.

This report describes the dosimeter and the way in which the data it returns may be used. The report is organized as follows: Section 2 is a description of the DMSP/F7 orbit. Section 3 is a description of the instrument and the data it returns. Section 4 describes the use of the data to obtain total dose and dose rate.

4. Gussenhoven, M.S., Hardy, D.A., Rich, F., Burke, W.J., and Yeh, H.-C. (1985) High-level spacecraft charging in the low-altitude polar auroral environment, J. Geophys. Res., 90:11009.

Section 5 describes the use of the data to obtain proton flux values. Section 6 describes the use of the data to obtain electron flux values. Section 7 describes the use of the star count channels. In Appendix A corrections to the LOLET channels for bremsstrahlung are discussed. In Appendix B we list interactive routines developed at the Air Force Geophysics Laboratory (AFGL) for using the dosimeter data.

2. THE DMSP/F7 ORBIT

The DMSP/F7 satellite was launched in November 1983, into a sun-synchronous circular polar orbit in the 1030 to 2230 local time meridian. It has an altitude of 840 km, an orbital period of approximately 101 min, and an inclination of 98.8°.

Because of the offset between the geographic and the geomagnetic poles the satellite orbits cover a significant portion of the polar cap and auroral regions each day. Figure 1 is a plot of the diurnal orbital coverage for the north and south poles plotted in corrected geomagnetic latitude (MLAT) and magnetic local time (MLT). For this figure the orbital position of the satellite over one day was projected down magnetic field lines to an altitude of 110 km using a Jensen-Cain model, and the envelope of the projection plotted.

The orbital paths for lower latitudes ($\pm 50^\circ$) are shown in geographic coordinates in Figure 2. The ascending and descending legs of three successive orbits are shown. Also indicated in Figure 2 is the region of the SAA. Approximately five successive orbits traverse different portions of the SAA twice per day.

3. THE DMSP/F7 DOSIMETER

The DMSP/F7 dosimeter, SSJ^{*}, measures the radiation dose from both electrons and protons, as well as the number of nuclear star events occurring behind four different thicknesses of aluminum shielding. In addition, it provides information on the differential and integral fluxes of electrons and protons at energies above the thresholds defined by the shields. The basic measurement technique is the determination of the amount of energy deposited in a simple solid-state detector from particles with sufficient energy to penetrate the omnidirectional aluminum shield of known thickness. Numerous detectors of this type have been flown since the early 1960's (Mozer et al;⁵ Paulikas and Freden;⁶ Gary and Cashion;⁷ and Grubb⁸). Most of these, however, have concentrated on measuring the integral flux of particles above the threshold, rather than dose. Only recently have results been reported for instruments that measure the dose from all types of radiation (Pruett⁹).

(Due to the large number of references cited above, they will not be listed here. See References, page 35.)

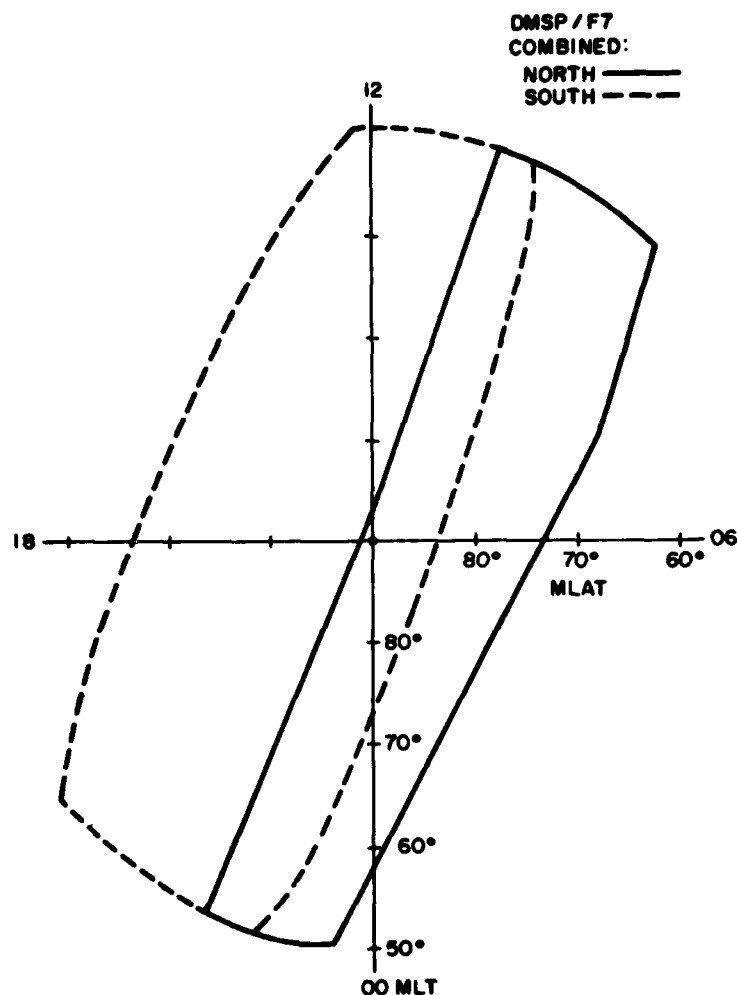


Figure 1. Diurnal Orbital Coverage for North and South Poles Plotted in Corrected Geomagnetic Latitude (MLAT) and Magnetic Local Time (MLT)

Figure 3 is a schematic drawing of one of the four sensors of the instrument (Sellers et al¹⁰). The solid state device selected as the active measuring element is a p-i-n diffused junction silicon semiconductor with a guard ring, having an energy deposition threshold of 50 keV. This allows the detection of both the high

10. Sellers, B., Kelliher, R., Hanser, F.A., and Morel, P.R. (1981) Design, Fabrication, Calibration, Testing and Satellite Integration of a Space-Radiation Dosimeter, AFGL-TR-81-0354, AD A113085, Air Force Geophysics Laboratory, Hanscom AFB, Massachusetts.

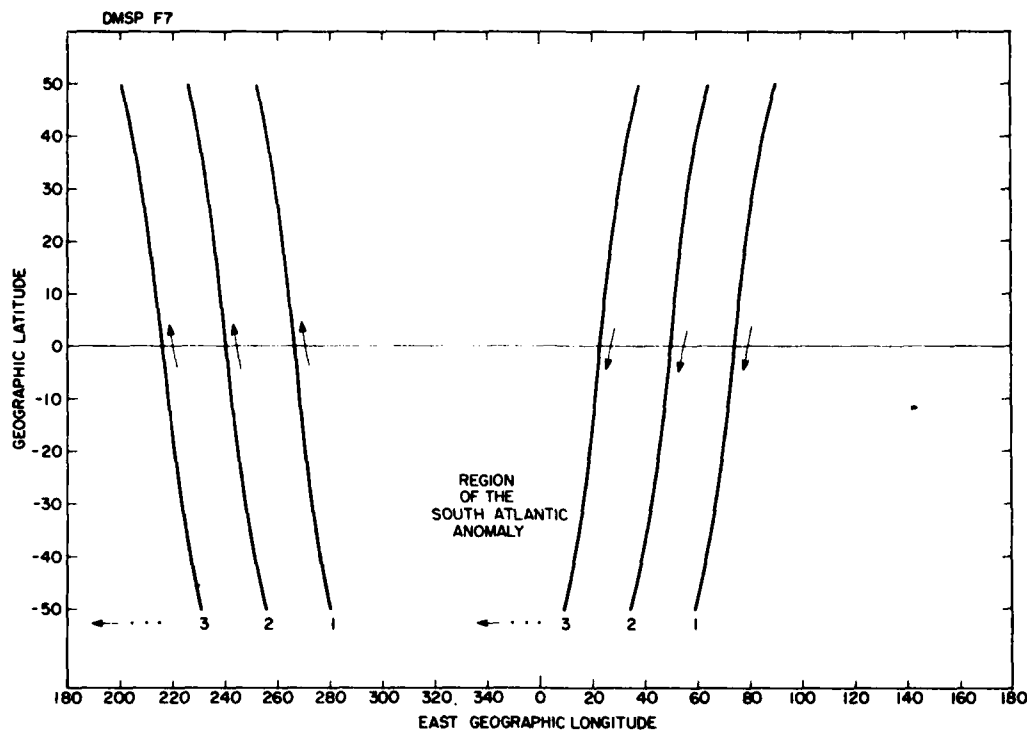


Figure 2. Satellite Path Across the Band of Geographic Latitudes From 50° to -50°

energy particles and most of the bremsstrahlung produced in the shield without compromising on-orbit lifetimes. Although many detectors in the past have used volume type devices whose detection area dimension is comparable to its thickness, the devices used in this detector are of the planar type with detection diameter large, compared to thickness. This choice was made in order to more nearly simulate real microelectronic components which are primarily planar.

Each detector is mounted behind one of the four hemispherical aluminum shields, or domes. The dome thicknesses increase with dome size and determine the four different incident particle energy thresholds for the detectors. They are 1, 2.5, 5, and 10 MeV for electrons, and 20, 35, 51 and 75 MeV for protons. The detector behind the 1 MeV shield has a detecting area of 0.051 cm^2 , and the remaining three have areas of 1.00 cm^2 . Particles which penetrate the shield and bremsstrahlung produced in the shield impact the active element and deposit energy in the device, producing a charge pulse. The charge pulse is shaped and amplified. The pulse height is proportional to the energy deposition in the detector. The characteristics

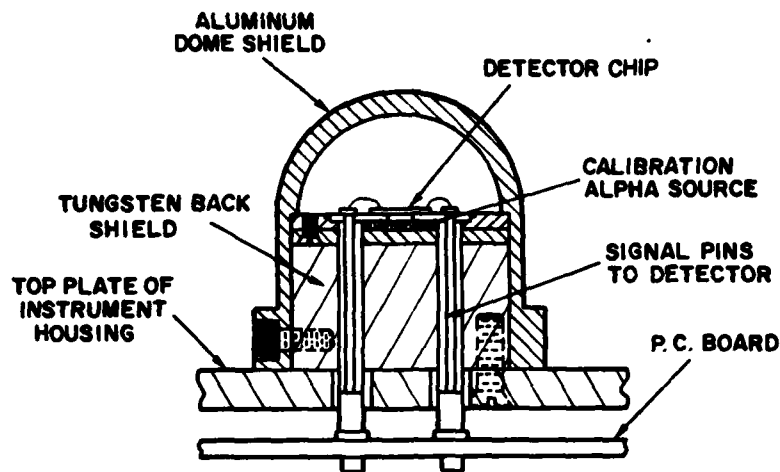


Figure 3. Schematic of One of the Four Sensors

of the detector and the threshold are such that energy depositions between 50 keV and 1 MeV are processed in four energy intervals to give the low linear energy transfer (LOLET) dose. Depositions between 1 MeV and 10 MeV are similarly processed for the high linear energy transfer (HILET) dose. Depositions above about 40 MeV in detectors 1, 2, and 4, and above 75 MeV in detector 3, are counted as very high linear energy transfer (VHLET) events, or nuclear star events. The LOLET dose comes primarily from electrons, high energy protons (above ~ 100 MeV incident), and bremsstrahlung. The HILET dose is primarily from protons below ~ 100 MeV incident. The VHLET dose comes from nuclear interactions (stars) initiated by high energy protons, from heavier cosmic rays, and from protons that traverse sufficiently long path lengths in the detectors.

The dose is taken to be directly proportional to the total energy deposited in the detector. Each pulse is analyzed to determine whether it will be counted for LOLET or HILET dose or a nuclear star event. The pulse height is then digitized and added to the sum of all other pulse heights measured in the accumulation interval (4 s). In addition, the total number of pulses measured in the accumulation interval is recorded in both LOLET and HILET channels. In the absence of significant bremsstrahlung, this number of counts can be used to determine the integral flux of electrons (LOLET) and ions (HILET) above the energy threshold determined by the aluminum shield. The very high thresholds of the VHLET channels were chosen to exceed normal incident angle proton energy losses. However, in regions of significant high energy protons which can deposit VHLET threshold energies as they traverse path lengths edgewise through the detectors, the star

channel can be used to determine differential proton fluxes in narrow energy windows.

To summarize, five separate outputs are obtained from each of the four hemispherically shielded detectors: HILET dose, LOLET dose, HILET flux counts, LOLET flux counts, and VHLET flux counts. The aluminum shields determine energy thresholds of 1, 2.5, 5, and 10 MeV for electrons, and 20, 35, 51, and 75 MeV for protons. A summary of the detector properties and their shieldings is given in Table 1.

Table 1. Design Parameters of Dome Sensors

Dome	Aluminum Shield (gm/cm ²)	Range Thresholds		Area (cm ²)	Detector Thickness (microns)
		Electrons (MeV)	Protons (MeV)		
1	0.55	1.	20	0.051	398
2	1.55	2.5	35	1.000	403
3	3.05	5.	51	1.000	390
4	5.91	10.	75	1.000	384

The SSJ^{*} dosimeter is located on the top of the DMSP satellite with the look direction always toward the zenith. This orientation insures a uniform average of trapped and cosmic ray particles independent of east-west effects (Filz and Holeman¹¹).

4. CALCULATION OF THE DOSE SPECTRA

The dosimeter distinguishes two levels of dose deposition behind each of the aluminum domes, LOLET and HILET. The LOLET channels respond to energy deposition from a single particle that falls in the range between 0.05 and 1 MeV. The HILET channels respond to energy deposition from a single particle that falls in the range between 1 and 10 MeV. If a single particle deposits more than 10 MeV in the detector it is not counted at all. Thus, a measurement of true total dose involves a correction for very high dose events. Fortunately, these are relatively rare. Generally, the total dose is simply the sum of the LOLET and HILET dose under each of the four domes. Plotting of the four doses versus shielding depth in gm/cm²

11. Filz, R. C., and Holeman, E. (1965) Time and altitude dependence of 55 MeV trapped protons, August 1961 to June 1964, J. Geophys. Res., 70:5806.

gives the depth dose spectrum for spherical shields. In principle it is also possible to determine the depth dose spectrum for slab shields. This would require a determination of the actual particle (proton and electron) spectra (see Sections 5 and 6) followed by a calculation of the energy deposited when the spectra are propagated through the slab. While the methods of determining the spectra and their accompanying uncertainties are addressed in the following sections, converting the spectra into slab shield depth dose is beyond the scope of this report.

The dose spectra are calculated by multiplying the dose counts in each channel by the appropriate calibration constant. These constants, taken from Sellers et al,¹⁰ are listed in Table 2. The LOLET dose calibration constants were determined using a Cs-137 source. Relativistic (1 to 10 MeV) electrons lose only about 200 keV, on average, in the detectors, so the Cs-137 spectrum, with an average energy loss near 200 keV, gives a good estimate of the electron response. The responses of the detector in Dome 1 to Cs-137 and Sr-Y-90 agree to within 2 percent. The HILET channel constants were determined using the digitizer level values for a flat spectrum. Since the proton energy loss spectrum is expected to be much broader than the electron energy loss spectrum, using the flat spectral value should give accurate results. Since the digitizers are reasonably linear, the actual values should not vary significantly with spectral shape. The calibration constants in Table 2 are estimated to be accurate to ± 10 percent for the particle environments expected to be encountered in the DMSP orbit.

Table 2. Channel Dose Calibration Constants

Channel	Calibration Constant LOLET	(Rads/Dose Count) HILET
D1	1.78×10^{-3}	1.36×10^{-4}
D2	1.81×10^{-4}	1.11×10^{-4}
D3	4.30×10^{-5}	2.90×10^{-5}
D4	4.85×10^{-5}	2.92×10^{-5}

The dosimeter is also calibrated periodically in-flight with a weak (~ 0.3 nCi) Am-241 source that emits ~ 5.5 MeV alpha particles. Between source and detector is a thin foil that changes the shape of the spectrum such that it peaks near 3 MeV and has a half-width of 1-2 MeV. In the normal mode of operation most pulses from the source will deposit enough energy that they will not appear in the LOLET window (0.05 to 1.0 MeV). The count rate from the source is 0.083, 0.0062,

0.029, and 0.027 c/s in the HILET dose channels 1 - 4, respectively, and a count rate of 0.000067, 0.000072, 0.00026, and 0.00019 c/s in the corresponding LOLET channels. Using the calibration constants in Table 2, the dose/day from the source is 0.97, 0.060, 0.073, and 0.068 rads/day in the HILET channels, and 0.010, 0.0011, 0.00096, and 0.00080 rads/day in the LOLET channels. For long-term dose accumulation or for short-term accumulation in regions of low relativistic fluxes, the corrections in the Dome 1 channels must be made. For instance, for days with no flare effects the correction to the HILET dose channel of Dome 1 is 46 percent of the total measurement.

During the calibration mode, two changes are made: (1) the amplifier gain is reduced by a factor of three which causes the alpha peak to straddle the HILET/LOLET threshold, and (2) the lower threshold is moved upward to the equivalent of 1 MeV (at the new gain setting). This increase in lower threshold allows the calibration to be made in the presence of much larger electron fluxes, since they will deposit much less energy than that required to trigger this level. Since the alpha peak is fairly narrow, it will require only a small gain shift to substantially change the HILET/LOLET flux ratio in the calibration mode.

One of the major strengths of the space radiation dosimeter is that it gives high resolution dose counts over short time intervals. The dose counts accumulated over 4 sec are called 'delta dose' counts. To survey the SSJ^{*} dose data we constructed plots of the average delta dose counts for each orbit. The averaging interval is 1 min, or 15 accumulation intervals. Figure 4 is a sample of the survey plots. The average delta dose counts are plotted for each of the four LOLET channels (labelled E1-E4) and each of the four HILET channels (labelled P1-P4) for the first full orbit on 3 February 1985. The scale is linear in counts and each channel output (including E1) has been advanced upward by five counts for separation of the channels from each other and from the abscissa. The counts are plotted as a function of time in UT seconds (each tick marks a 1-min interval), and as a function of satellite position in geographic latitude and longitude. The plot starts at the geographic equator, advances first toward the northern polar region, returns to the equator, proceeds to the southern polar region, and returns again to the equator.

In Figure 4 significant dose accumulation occurs in all channels as the satellite passes directly through the heart of the SAA (refer to Figure 2). In the lowest energy LOLET channel, small but clearly discernible dose counts are also measured in the high latitude regions which map to the electron outer zone. Because of the relatively large calibration constant for this channel, these small counts also represent a significant dose. The total dose obtained from the traversal of the SAA for the four shielding thicknesses is obtained by summing the delta dose

DMSP

3 FEB85

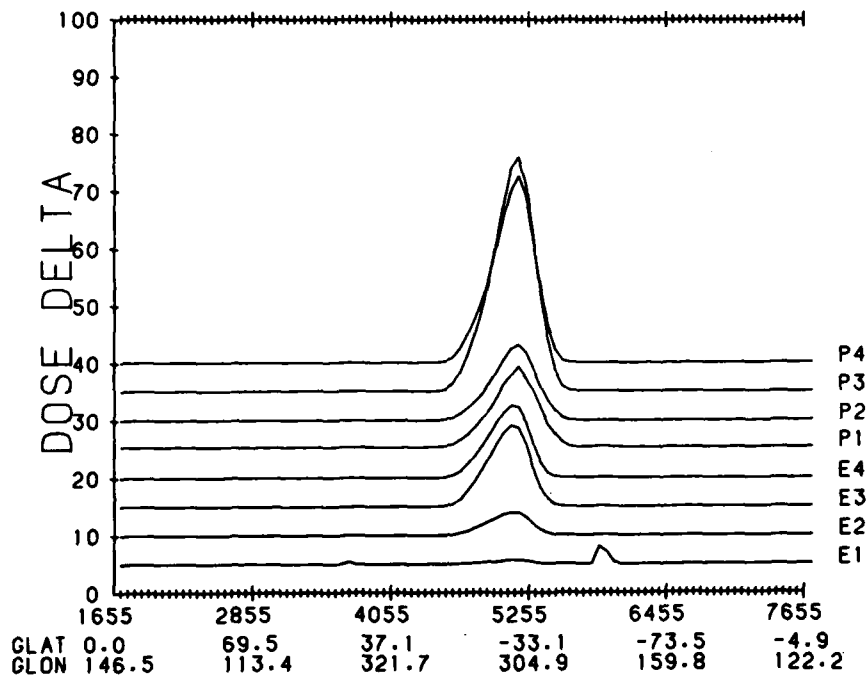


Figure 4. Survey Plot of Delta Dose Counts for the First Full Orbit on 3 February 1985

counts from 4355 to 5735 UT in each of the channels and by applying the constants in Table 2. The resulting depth dose spectra are shown in Figure 5 for the LOLET, HILET and total dose. The spectra are hard, falling only somewhat more than a factor of two over the entire shielding range, and approaching saturation for the thickest shielding. The HILET dose is approximately twice the LOLET dose. The total dose behind the thinnest (thickest) shield is 0.38 (0.17) rads. In five such passes through the SAA (the approximate number per day of equivalent passes) the total dose per day from the SAA is nearly 2 (1) rads behind the thinnest (thickest) shield.

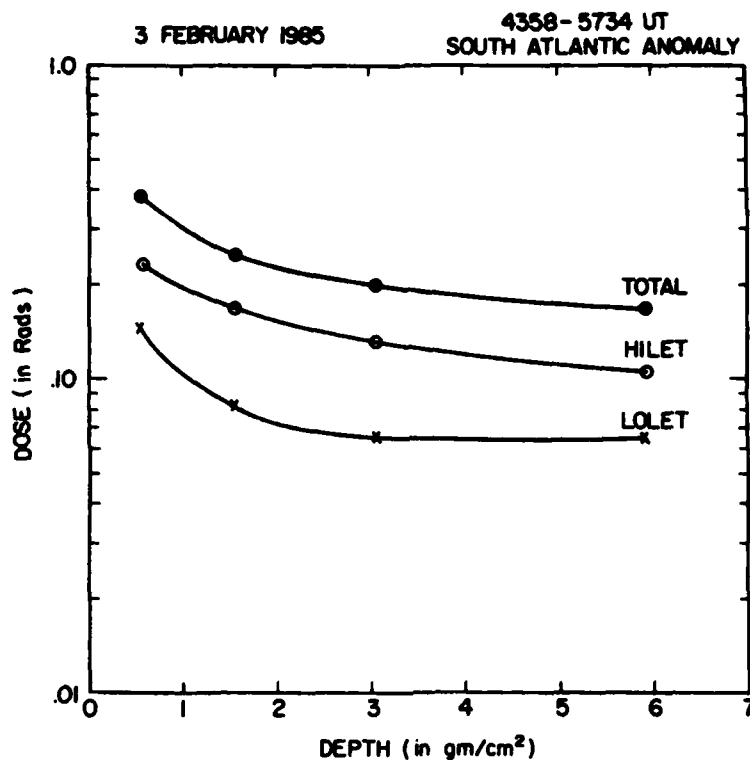


Figure 5. Depth Dose Spectra for Passage Through the Heart of the SAA on 3 February 1985 From 4355 to 5735 UT. HILET, LOLET and total dose are plotted separately

5. CALCULATION OF THE RESPONSE FUNCTION FOR PROTON FLUX SPECTRA

Figure 6 is the survey plot of flux counts corresponding to the delta dose plot in Figure 4. Again the flux counts per 4-sec accumulation time are averaged over 1-min intervals. The flux counts for the HILET (LOLET) channels are labelled P1-P4 (E1-E4). The counts for each channel are advanced one decade from the preceding channel, starting with P2. In addition to flux counts from the SAA, occurring in all channels, the outer zone electron fluxes are clearly evident in the LOLET channels as four peaks at northern and southern high latitudes. The fluxes in the E1 channel are the source of the dose counts in the E1 channel in Figure 4 outside the SAA.

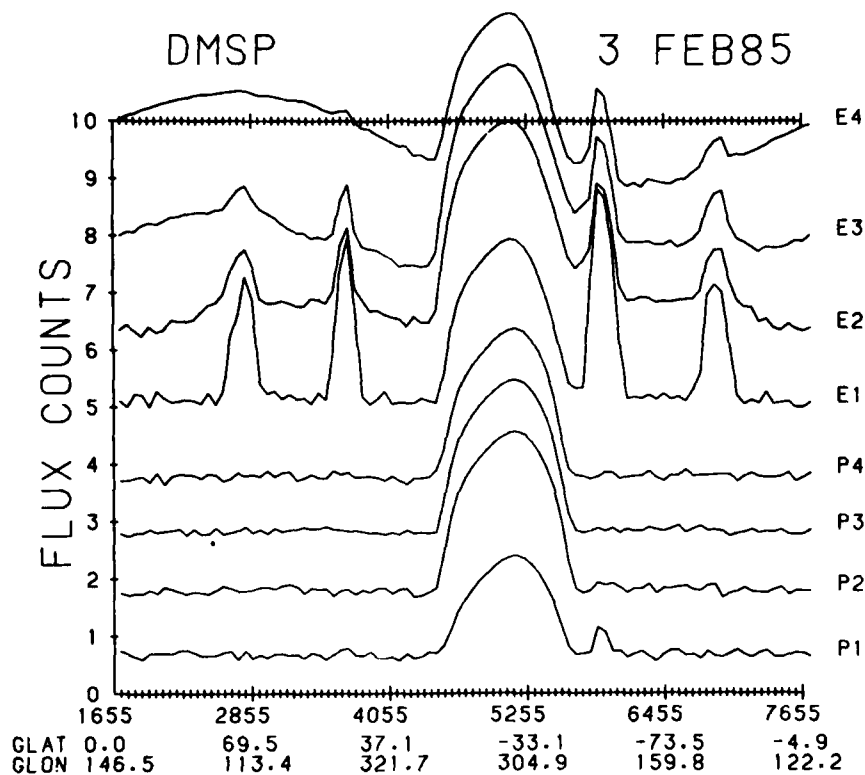


Figure 6. Survey Plot of Flux Counts for the First Full Orbit on 3 February 1985

The process of converting flux and dose counts to integral or differential flux is not a straightforward one. We describe here a method for calculating the geometric factors for two types of proton distributions: isotropic and trapped. In general, the geometric factor, $\{dg(\theta)/d\theta\} d\theta$, for an energetic particle detector is the area solid angle factor (in $\text{cm}^2 \text{sr}$). It is used to compute the directional differential flux $j(E, \theta)$ (in $\text{particles}/\text{cm}^2 \text{s sr MeV}$) from the instrument counting rate, CR (in counts/s), for a channel with central energy E , and width ΔE . Or alternatively, we may write:

$$\text{CR} = \int_E \int_{\theta} j(E, \theta) \{dg(E, \theta)/d\theta\} dE d\theta. \quad (1)$$

If the differential flux can be expressed as a separable function in energy and angle:

$$j(E, \theta) = j(E)h(\theta), \quad (2)$$

then

$$CR = \int_E j(E) \left\{ \int_{\theta} h(\theta) dg/d\theta d\theta \right\} dE . \quad (3)$$

Or

$$CR = \int_E j(E) G(E) dE , \quad (4)$$

where

$$G(E) = \int_{\theta} h(\theta) dg/d\theta d\theta . \quad (5)$$

For the DMSP dosimeter the energy width of an individual channel is broad enough, and the change in typical $j(E)$ large enough over the effective energy width of the channel, that we cannot avoid having to perform the energy integral in Eq. (4) to relate the count rate to the differential flux. To do this a spectral shape must be assumed. Also, the geometric factor, $G(E)$, is so strongly dependent on angular distribution that it is impossible to assign a single geometric factor that will apply in all cases.

Here we use a new method of deriving trapped proton fluxes which maximizes the amount of information available from a detector with a large opening angle. The method is derived from the calculations of Freden and Paulikas¹² but generalizes their technique to multiple instruments and unknown energy spectra. The method, as applied to the DMSP dosimeter, draws heavily on the infinite slab approximation to the silicon detector and the similarity of the four instruments (domes). The energy dependent geometric factor, or the response function, is calculated for two types of energetic proton angular distributions: isotropic and mirror plane. The two distributions are chosen to represent relativistic particles at high latitudes during solar flares and protons in the SAA, respectively. For each of these two angular distributions, we compute the geometric factor of the detector for a given intensity of monoenergetic protons. The spherical symmetry (energy loss independent of direction) of the dome coupled with the cylindrical symmetry (path length independent of azimuthal angle) of the silicon detector allows direct integration of the response function for each energy of interest.

The response of the detector, $\{ dg/d\theta \} d\theta$, to a flux of particles $j(E, \theta)$ of energy E and incident to the normal to the detector surface at angle θ is:

12. Freden, S. C., and Paulikas, G. A. (1964) Trapped protons at low altitudes in the South Atlantic Magnetic Anomaly, J. Geophys. Res., 69:1259.

$$\{dg/d\theta\} d\theta = A \cos \theta d\Omega \quad (\text{cm}^2 \text{ sr}) \quad (6)$$

where A is the detector area, θ is the angle to the detector normal, and $d\Omega$ is the element of solid angle centered on θ . Then, for angular distribution $h(\theta)$ the energy dependent geometric factor $G(E)$ is:

$$G(E) = \int_{\Omega} A h(\theta) \cos \theta d\Omega . \quad (7)$$

Here $h(\theta)$ is either unity for the isotropic distribution, or a delta function for the trapped mirror plane distribution. These will be discussed in more detail below. In Eq. (7) the limits of integration are not over the entire solid angle, but only over those angles (from θ_1 to θ_2) for which a proton with incident energy, E , will deposit the prescribed energy: from 1 to 10 MeV for the HILET channels, or from 0.05 to 1 MeV for the LOLET channels. The limits of integration are determined by using the range-energy relationship

$$R(\text{silicon}) = 11.824 \cdot E^{1.772518} \quad (8)$$

of Bischel and Tschalaer¹³ in the infinite slab approximation. In Eq. (8), R is in microns, and E is in MeV. The limits of integration for Eq. (7) then, are energy dependent.

The geometric factor, $G(E)$, for incident proton energy in 1 MeV intervals from 1 to 1000 MeV is computed for the two types of angular distribution. Next, we assume a spectral shape for the distribution in energy $j(E)$. By integrating Eq. (4) over the appropriate energy width of a given channel, we then have the relationship between the counts in the channel and a reference flux of the distribution.

For instance, for a flat distribution in energy, j_0 ($j(E)$ independent of energy):

$$G_0 = \int_E G(E) dE = CR(\text{flat})/j_0 . \quad (9)$$

Here G_0 is the energy independent geometric factor. Since the dosimeter has twenty different channels (counting flux, dose and star channels separately) each giving a count rate over a different energy interval, there are twenty values of G_0 , and therefore, twenty ways to calculate the same j_0 for the assumed flat spectrum.

13. Bischel, H., and Tschalaer, C. (1967) A range-energy table for heavy particles in silicon, Nuclear Data, Section A, 3:343.

A more appropriate energy distribution for the relativistic protons measured in the DMSP orbit is a power law spectrum, with spectral index N:

$$j(\theta, E) = j(20) h(\theta) (20/E)^N, \quad (10)$$

where $j(20)$ is the value of the differential flux at 20 MeV (the lowest energy measured for protons) and $h(\theta)$ is one of the two assumed angular distributions discussed above. For each channel, then, the energy independent geometric factor $G(N)$, in $\text{cm}^2 \text{ sr MeV}$, is given by

$$G(N) = \int_E G(E) (20/E)^N dE = CR/j(20). \quad (11)$$

The integration is performed from the threshold energy of the channel to infinity. As was the case for the flat spectrum, dividing the twenty values of $G(N)$ into the twenty appropriate counting rates will give twenty values of $j(20)$. If the correct value of N were used, all values will be the same. Any deviation must come from a more complicated energy spectrum or angular distribution, or from the presence of other particles, such as electrons or alpha particles. To obtain the proton spectrum, then, we simply vary N until the best agreement is found among all values of $j(20)$, and use these values of $j(20)$ and N in Eq. (10).

In practice the LOLET channels are not useful for calculating proton fluxes since there is almost always a real electron flux contributing to the count rate, and the star channels are also not of great use unless there is a significant flux of very high energy protons. This leaves the HILET flux and dose counts, or eight channels, for determining the proton spectra.

Isotropic Proton Distribution Response. For solar flare particles one generally assumes an isotropic distribution. However, since some of the higher energy particles will be excluded from a significant portion of the upcoming hemisphere, this leads to ambiguities in the determination of the absolute omnidirectional flux. For an isotropic distribution the function $h(\theta)$ in Eqs. (7) and (10) is taken to be unity. Also, because the distribution is isotropic we will calculate the final energy independent geometric factors for an omnidirectional differential flux, $j(E)$, in $\text{p/cm}^2 \text{ s MeV}$. Thus, $G(N)$ will be in $\text{cm}^2 \text{ MeV}$, and derived from the directional energy independent geometric factor by dividing by $4\pi \text{ sr}$.

The calculation of the energy-dependent geometric factor, $G(E)$, for the bare detector measuring HILET flux counts is straightforward from Eq. (7) once the limits of integration are determined for each energy of interest. Figure 7 shows the minimum (dashed line) and maximum (solid line) angles for a bare detector with HILET energy deposition (1 to 10 MeV) for incident energies from

1 and 1000 MeV. Between 1 and 10 MeV, the entire solid angle integration is used. The maximum LOLET limit for protons is given by the dashed line in Figure 7. The minimum angle is zero.

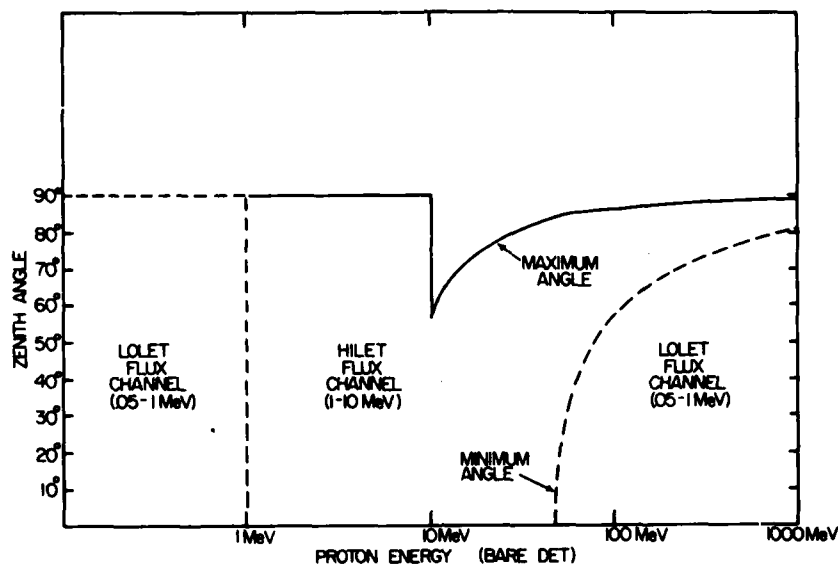


Figure 7. Limits of Integration for the Energy Dependent Geometric Factor for Protons. For HILET channels and energies between 1 and 1000 MeV, the maximum (minimum) angle is given by the solid (dashed) line. For the LOLET channels, over the entire energy range, the maximum angle is given by the dashed line and the minimum angle is zero.

To show the effects of the integration limits on Eq. (7) the energy dependent geometric factor, $G(E)$, is first calculated for a bare silicon detector of thickness $400\ \mu$ and for energy deposition between 1 and 10 MeV (HILET channels). Calculations for the flux counts and the dose counts differ by the use of a weighting factor in the latter case (see Sellers et al.¹⁰). The resulting $G(E)$ for the HILET dose channel is shown in the first curve in Figure 8. The primary response is below 100 MeV, while the contribution at higher energy would only be significant if the spectrum were very flat (or increased with energy, as the galactic cosmic ray spectrum does in this energy range).

The actual response for each of the four DMSP dosimeter HILET dose channels to an incident energy is modified by the presence of the dome shields. The external

energies required to penetrate the domes and give the resultant internal energies are presented in Table 3. The four curves in Figure 8 marked 1-4 are the energy dependent geometric factors for the 400- μ detector behind domes 1 to 4, respectively. The values for dome 1 must be additionally divided by 19.6, since the detector area is reduced by this amount (Table 1). The effect of the domes on the response function is to make the energy window of the response fairly narrow in incident particle energy.

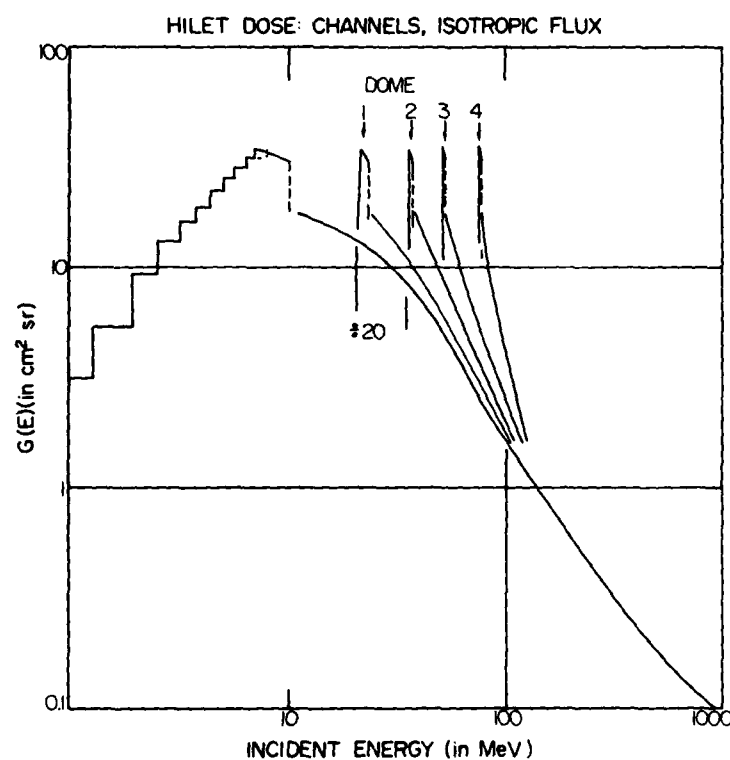


Figure 8. Response Function for a 400 μ Silicon Detector to a Flat Proton Spectrum Which is Isotropic and Has Unit Flux, for Incident Energies Between 1 to 1000 MeV and for Energy Deposition of 1 to 10 MeV (first curve), and Response Functions to the Same Spectrum for the Detector Behind Domes 1, 2, 3, and 4. These response functions apply to the HILET dose channel

Table 3. Internal vs External Proton Energy for Different Domes

Internal Proton Energy (MeV)	External Proton Energy (MeV)			
	Dome 1	Dome 2	Dome 3	Dome 4
0	20.0	35.0	51.0	75.0
8	21.8	37.0	52.5	75.2
10	23.4	37.8	53.0	75.7
20	30.0	43.0	56.8	78.5
40	45.0	55.0	68.0	87.5
100	103.2	110.0	119.0	124.2
1000	1001.	1003.	1005.	1010.

The energy independent geometric factors, $G(N)$ in $\text{cm}^2 \text{ MeV}$, have been computed for all 20 channels of the DMSP dosimeters for an isotropic proton flux with power law energy spectral exponents, N in Eq. (10), of 0.1 to 10.0. They are given in Table 4a (for the eight flux channels) and Table 4b (for the eight dose channels) in varying steps of N , from 0.1 to 10. The geometric factors, $G(N)$, for the HILET flux and dose channels are plotted in Figures 9a and 9b, respectively, showing that interpolation between points listed in Table 4 is clearly warranted. The counting rates of any channel divided by the geometric factor gives the omnidirectional differential proton flux ($p/\text{cm}^2 \text{ s MeV}$) at 20 MeV with the necessary spectral index, N , to give that counting rate. If the proton spectrum has this form (isotropic angular distribution and power spectral energy distribution) and the individual channel counting rates are divided by their respective geometric factors, then the same flux at 20 MeV will result.

As an illustrative example we apply this method to the average of counts across the northern polar cap at the peak of a solar flare event on 16 February 1984. The survey plots of flux and dose counts are shown in Figures 10a and 10b, respectively. In these plots the SAA is evident from $\sim 39,400$ UT to the end of the pass. The two outer zone electron peaks for each hemisphere that were so apparent in Figure 6 now occur at the outer edges of high level fluxes across each of the polar caps ($\sim 35,160$ to $36,360$ UT in the north pole, and $\sim 37,980$ to $39,360$ UT in the south pole). Significant dose counts are measured in both the LOLET and HILET dose channels over these same regions (Figure 10b). The fluxes that reach these high latitudes accompanied a solar flare that began at ~ 09 UT ($32,400$ UT). Strong flare effects in the vicinity of the Earth were short-lived (< 10 hr), but the flare was intense enough to produce ground level neutron signatures. Integral proton

fluxes of $6 \cdot 10^2$ p/cm² s sr for energies greater than 10 MeV were reported from the GOES-6 satellite in geosynchronous orbit at the peak of the event (Preliminary Report and Forecast of Solar Geophysical Data, 1984).

Table 4a. Omnidirectional Geometric Factors of the Flux Channels for Protons in (cm² MeV)

N	P1	P2	P3	P4	E1	E2	E3	E4
0.10	3.096	55.95	48.49	42.36	29.27	569.0	566.0	557.1
0.20	2.671	47.20	40.23	34.44	21.37	414.8	412.1	404.5
0.30	2.325	40.10	33.56	28.12	15.67	303.6	301.2	294.6
0.40	2.040	34.29	28.15	23.06	11.54	223.1	221.0	215.4
0.50	1.804	29.49	23.72	18.98	8.543	164.8	162.8	158.0
0.60	1.607	25.50	20.08	15.68	6.354	122.2	120.5	116.4
0.70	1.441	22.17	17.07	13.00	4.751	91.08	89.56	86.06
0.80	1.300	19.36	14.57	10.80	3.572	68.22	66.88	63.88
0.90	1.179	16.97	12.47	9.005	2.701	51.37	50.19	47.62
1.00	1.075	14.94	10.71	7.525	2.054	38.89	37.84	35.64
1.10	.9851	13.20	9.225	6.303	1.572	29.59	28.68	26.79
1.20	.9064	11.70	7.966	5.291	1.210	22.65	21.84	20.23
1.30	.8373	10.41	6.896	4.450	.9368	17.43	16.72	15.33
1.40	.7764	9.267	5.983	3.749	.7300	13.49	12.87	11.68
1.50	.7224	8.280	5.201	3.164	.5723	10.50	9.949	8.929
1.60	.6742	7.415	4.529	2.674	.4514	8.213	7.733	6.857
1.70	.6312	6.655	3.951	2.263	.3582	6.461	6.040	5.288
1.80	.5925	5.984	3.452	1.918	.2859	5.110	4.740	4.095
1.90	.5577	5.391	3.021	1.628	.2295	4.063	3.738	3.184
2.00	.5262	4.865	2.647	1.383	.1853	3.246	2.961	2.485
2.20	.4715	3.980	2.039	1.001	.1226	2.102	1.883	1.531
2.40	.4251	3.274	1.578	.7267	.0827	1.386	1.217	.9565
2.60	.3874	2.707	1.226	.5294	.0568	.9281	.7978	.6054
2.80	.3547	2.248	.9557	.3877	.0396	.6306	.5302	.3877
3.00	.3265	1.874	.7472	.2832	.02798	.4340	.3565	.2509
3.50	.2714	1.207	.4084	.1311	.01234	.1786	.1381	.0879
4.00	.2313	.7921	.2262	.0614	.00575	.0774	.0562	.0322
4.50	.2010	.5270	.1266	.0289	.00279	.0349	.0237	.0122
5.00	.1776	.3550	.0716	.0138	.00140	.0162	.0103	.0047
6.00	.1436	.1659	.0233	.0032	.00037	.0037	.0021	.0008
7.00	.1201	.0800	.0078	.0007	.00011	.0008	.0004	.0001
8.00	.1029	.0394	.0027	.0002	.00003	.0002	.0001	.0000
9.00	.0897	.0198	.0008	.0000	.00001	.0001	.0000	.0000
10.00	.0792	.0101	.0003	.0000	.00001	.0000	.0000	.0000

Figure 4b. Omnidirectional Geometric Factors of the Dosim Channels for Protons in (cm² MeV)

N	P1 multiply by x10 ⁻³	P2 x10 ⁻³	P3 x10 ⁻³	P4 x10 ⁻³	E1 x10 ⁻⁵	E2 x10 ⁻⁴	E3 x10 ⁻³	E4 x10 ⁻³
0.10	129.8	144.3	495.1	427.2	1531.	1495.	576.1	554.2
0.20	113.6	123.1	414.5	349.7	1158.	1127.	433.5	415.0
0.30	100.2	105.8	349.0	287.6	880.9	854.3	327.8	312.0
0.40	89.15	91.46	295.4	237.4	673.9	650.9	249.1	235.8
0.50	79.88	79.52	251.2	196.8	518.6	498.6	190.2	178.7
0.60	72.06	69.51	214.5	163.6	401.5	384.0	146.0	136.1
0.70	65.39	61.05	183.9	136.5	312.6	297.4	112.6	104.1
0.80	59.67	53.85	158.3	114.2	244.9	231.5	87.31	79.98
0.90	54.72	47.68	136.6	95.76	193.0	181.2	68.01	61.70
1.00	50.40	42.37	118.3	80.51	152.9	142.6	53.24	47.79
1.10	46.61	37.78	102.7	67.84	121.9	112.8	41.87	37.17
1.20	43.26	33.77	89.34	57.27	97.68	89.67	33.08	29.02
1.30	40.29	30.28	77.91	48.44	78.70	71.63	26.25	22.74
1.40	37.63	27.20	68.08	41.03	63.74	57.49	20.92	17.89
1.50	35.25	24.50	59.60	34.82	51.89	46.36	16.75	14.12
1.60	33.09	22.10	52.26	29.58	42.44	37.54	13.46	11.18
1.70	31.15	19.98	45.90	25.16	34.87	30.53	10.85	8.960
1.80	29.38	18.09	40.36	21.43	28.77	24.92	8.784	7.083
1.90	27.76	16.41	35.54	18.28	23.84	20.42	7.134	5.662
2.00	26.28	14.90	31.33	15.60	19.83	16.80	5.813	4.539
2.20	23.67	12.33	24.43	11.39	13.86	11.47	3.895	2.940
2.40	21.44	10.26	19.12	8.348	9.820	7.930	2.638	1.922
2.60	19.52	8.563	15.01	6.134	7.037	5.541	1.804	1.268
2.80	17.85	7.174	11.82	4.518	5.094	3.908	1.245	.842
3.00	16.40	6.028	9.332	3.334	3.721	2.779	.865	.564
3.50	13.45	3.947	5.216	1.573	1.753	1.222	.359	.212
4.00	11.22	2.620	2.947	.749	.858	.557	.154	.092
4.50	9.495	1.757	1.680	.359	.432	.261	.067	.032
5.00	8.125	1.189	.964	.173	.223	.125	.030	.013
6.00	6.110	.5557	.323	.041	.062	.030	.006	.002
7.00	4.721	.2653	.110	.010	.018	.008	.001	.000
8.00	3.722	.1288	.038	.002	.006	.002	.000	.000
9.00	2.981	.0633	.013	.000	.002	.001	.000	.000
10.00	2.417	.0314	.005	.000	.001	.000	.000	.000

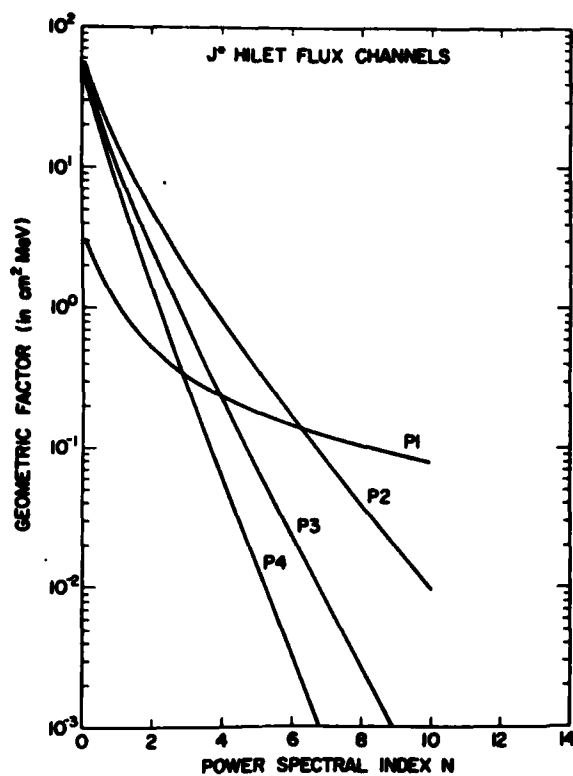


Figure 9a. Energy Independent Geometric Factors for Protons as a Function of the Power Spectral Index for the HILET Flux Channels

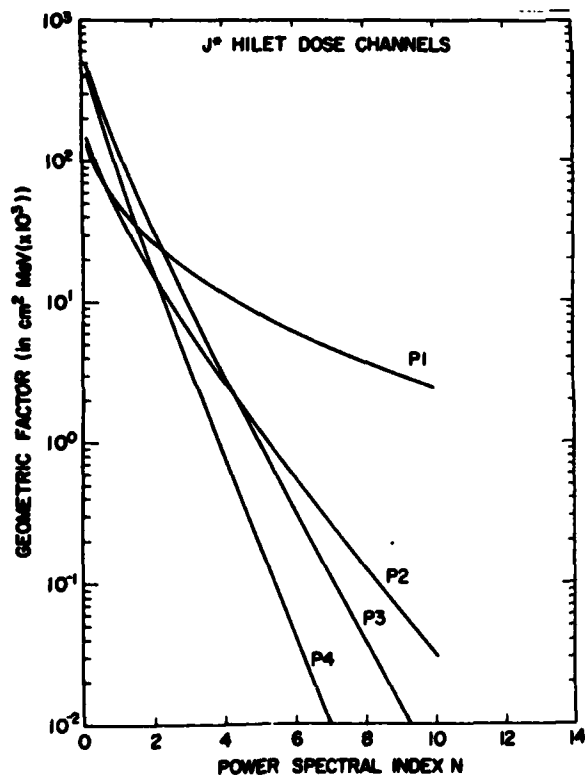


Figure 9b. Energy Independent Geometric Factors for Protons as a Function of the Power Spectral Index for the HILET Dose Channels

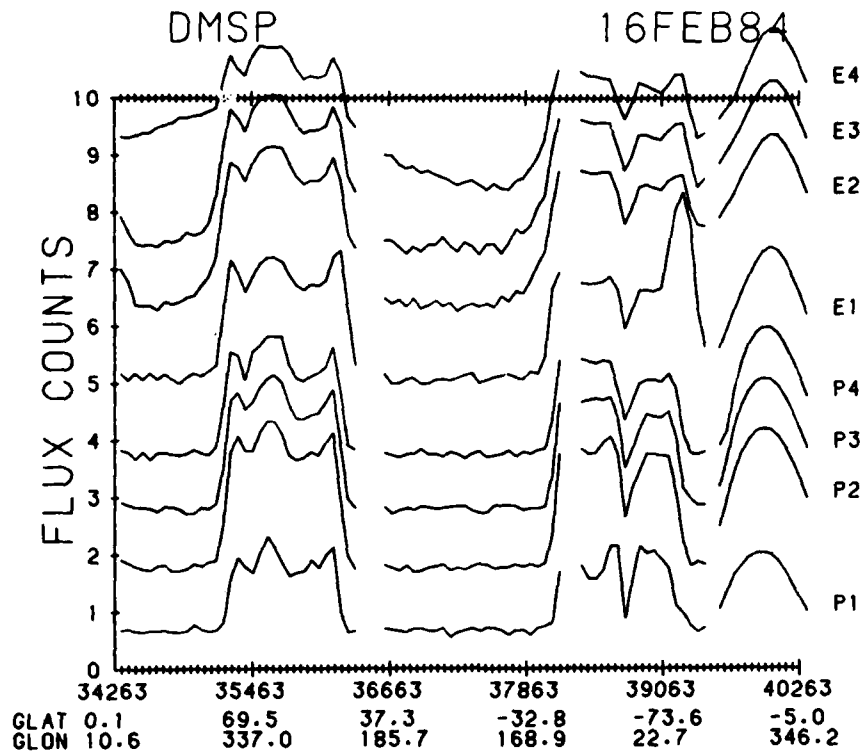


Figure 10a. Survey Plots for the J* Dosimeter for 16 February 1984 Showing Flux Counts

A listing of the average count rates and standard deviations for each of the HILET and LOLET channels for a 1-min interval at the peak of the particle precipitation (35,596 to 35,656 UT) is given in Table 5. The total star counts for this interval are also listed. Because the flare particles include electrons, as well as protons, we use only the HILET flux and dose counts to find the power spectral index that minimizes the difference in $j(20)$. An estimate of the value of N can be obtained by inspection of the ratios of the counts and the cross-overs of the $G(N)$ curves in Figures 9a and 9b. For instance, since the Dome 2 and Dome 4 HILET dose count rates are approximately the same, they will only give the same $J(20)$ if the values of $G(N)$ for these two channels are the same. Figure 9b shows that this occurs at $N \sim 2$. Table 6 gives the values of $j(20) = CR/G(N)$ for three values of N : 1.7, 1.8, and 1.9. For each dome the HILET flux count (dose counts) are listed without (with) parentheses. Errors carried over from the standard deviation in the average are also listed. The flux counts are very sensitive to N . Here, $N = 1.8$ gives the best agreement, with all points falling well within

DMSP

16FEB84

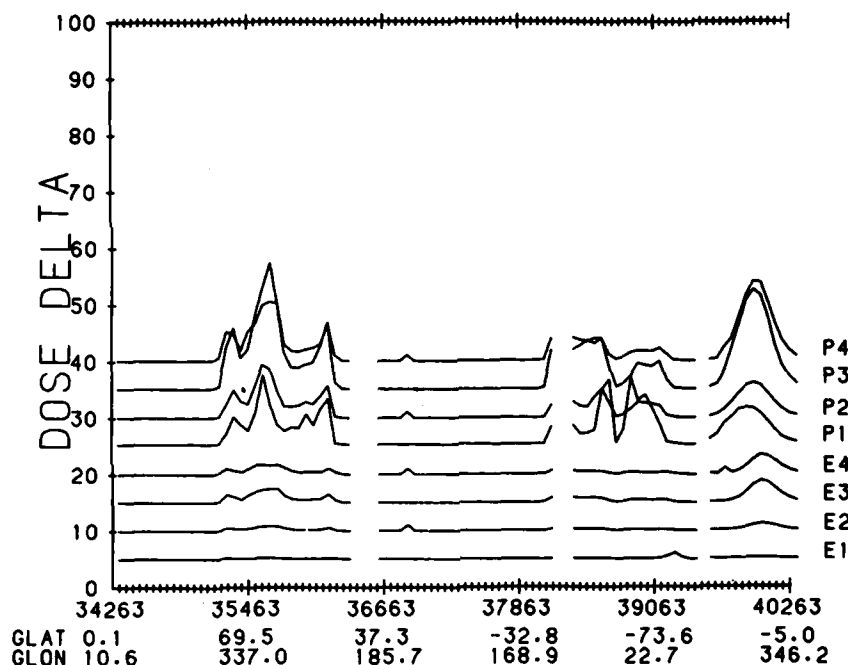


Figure 10b. Survey Plots for the J* Dosimeter for 16 February 1984 Showing Dose Counts

the standard deviation. Good agreement is also found for this value of N between the dose channels, but the dose value for $j(20)$ is uniformly higher than that from the flux counts. This trend holds generally. We use the flux counts to determine $j(20)$. They are larger, have smaller statistical errors, and their geometric factors are more directly obtained (no weighting factors are required). We use the dose channels to check for consistency.

Thus, using all flux channel results to obtain the best average value of $j(20)$ for $N = 1.8$, we conclude that the best spectral fit for these data is:

$$j(E) = 86(\pm 2) \cdot \{20/E\}^{1.8} \text{ p/cm}^2 \text{ s MeV} , \quad (12)$$

where E is in MeV. Here, we have used the standard deviation in the values of $j(20)$ as the error. Under the assumption of complete isotropy at DMSP altitudes, and integrating over energy from 10 MeV to infinity, the directional integral flux from Eq. (12) is $298 \text{ p/cm}^2 \text{ s sr}$. This is one-half the peak value measured at geosynchronous orbit by GOES-6. We consider this to be reasonably good agreement.

Table 5. Average Count Rates (c/s) on 16 February 1984 From 35,596 to 35,656 UT

Channels	Dome 1	Dome 2	Dome 3	Dome 4
HILET Flux	50.8 \pm 6.3	532.0 \pm 40.0	295.0 \pm 22.0	163.0 \pm 12.0
HILET Dose	3.13 \pm 0.58	2.33 \pm 0.24	4.50 \pm 0.43	2.48 \pm 0.19
LOLET Flux	39.8 \pm 3.0	342.0 \pm 21.0	263.0 \pm 25.0	192.0 \pm 18.0
LOLET Dose	0.0313 \pm 0.086	0.19 \pm 0.11	0.56 \pm 0.17	0.41 \pm 0.16
Total Star Count	0	7	1	5

Table 6. J(20): Count Rate/G(N) in P/(cm² s MeV) From 35,596 to 35,656 UT on 16 February 1984

N	Dome 1	Dome 2	Dome 3	Dome 4
1.7	81 \pm 10 (100 \pm 19)	80 \pm 6 (117 \pm 12)	75 \pm 6 (98 \pm 9)	72 \pm 5 (99 \pm 8)
1.8	86 \pm 11 (107 \pm 20)	89 \pm 7 (129 \pm 13)	85 \pm 6 (111 \pm 11)	85 \pm 6 (116 \pm 9)
1.9	91 \pm 11 (113 \pm 21)	99 \pm 7 (142 \pm 15)	98 \pm 7 (126 \pm 12)	100 \pm 7 (135 \pm 10)

Trapped Mirror Plane Proton Response. In addition to solar flare protons, which are assumed to be isotropic in angular distribution, the other major population of protons at the DMSP altitude is trapped in the radiation belt and reaches low altitudes in the SAA. A mirror plane angular distribution is appropriate for these particles. In the mirror plane geometry the particles are assumed to be contained wholly in the plane but with a uniform distribution around the plane, that is, the angular distribution function is a delta function about the mirror plane. For the DMSP orbit the trapped protons are contained within $\sim 16^\circ$ of the mirror plane, and since the detector axis points toward the zenith, the east-west asymmetry of the protons does not have to be additionally taken into account. (See Filz and Holeman¹¹ for both effects.) Thus, in calculating the geometric factor it is only necessary to account for the angle between the mirror plane and the detector plane, which is 90° minus the magnetic dip angle (inclination). For the SAA, at the low altitudes considered here, the dip angles do not exceed $\sim 60^\circ$. At these inclinations we will show that the geometric factor varies relatively slowly with angle (see below). For

these reasons, the delta function mirror plane angular distribution is a good approximation to the proton distributions in the SAA.

The relative response of the HILET dose channel for an unshielded silicon detector, to mirroring protons of energies greater than 10 MeV, is shown as a function of magnetic dip angle in Figure 11. For each angle there is a large response in the 10-MeV range, and a more slowly varying response for larger energies. Table 7 lists response function values for a sampling of energies for every 10° in magnetic inclination. The values are normalized by pi times the area of the detector. The complex response shown in the table and in Figure 11 results from a combination of the onboard dose calculation and the interaction of the energy loss/geometric factor angular dependence. The sharp falloff towards 90° comes from the cosine factor and delta function pitch angle dependence assumed. Obviously, for inclinations greater than ~80° a more accurate calculation is required and the entry of particles from the sides of the detector must be included. The sharp cutoff of lower energy protons is a result of the maximum energy loss acceptance of 10 MeV. The fact that particles in a certain energy range are not counted, while these are small, must be corrected for in precision dose calculations.

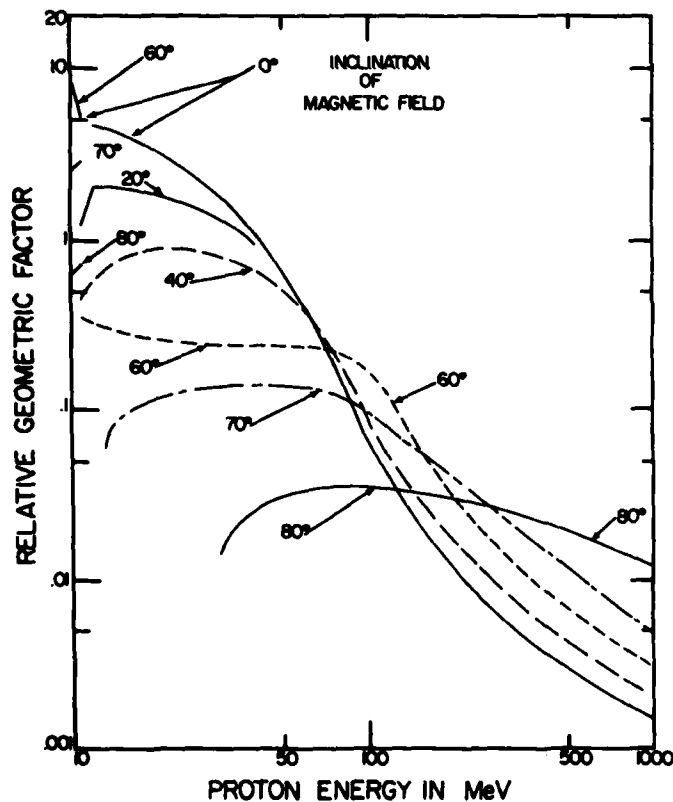


Figure 11. Relative Response Function for Protons of an Unshielded 400 μ Silicon Detector for the Trapped Mirror Plane Distribution at Different Values of the Magnetic Field Inclination

Table 7. Response Function of 400 μ Bare Silicon Detector to a Delta Function Trapped Mirror Plane Distribution in the Infinite Slab Approximation (HILET Dose Channel) (Normalized by $\pi \cdot \text{Area}$)

Energy in MeV	Magnetic Inclination									
	0	10	20	30	40	50	60	70	80	
8	4.0005	3.7406	3.8557	4.3047	4.2865	2.8075	1.6077	0.7232	0.1823	
10	1.6549	1.6907	1.4549	1.4807	1.5173	1.8352	2.0096	0.9046	0.2279	
10.01		0.69	0.39	0.31	0.15	0.069	0.00	0.00	0.00	
11	1.4847	1.0476	0.6152	0.2975	0.1828	0.0938	0.0112	0.00	0.00	
20	0.9463	0.7083	0.4740	0.2912	0.2866	0.1524	0.0825	0.0389	0.00	
40	0.3892	0.3352	0.3048	0.3942	0.2227	0.1155	0.0779	0.0448	0.0085	
100	0.0201	0.0205	0.0216	0.0239	0.0279	0.0361	0.0536	0.0309	0.0112	
300	0.0022	0.0022			0.0028		0.0045		0.0080	
1000	0.00048	0.00049	0.00052		0.00063		0.00098	0.00148	0.00380	

The energy dependent response function of the unshielded detector for the HILET dose channel for a magnetic inclination of 40° is shown in Figure 12. Also shown in Figure 12 are the response functions for the four different dome shields. (Again, a reduction by a factor of 20 is necessary for the small detector behind Dome 1.) Figure 12 shows that the HILET dose channel response is significant only in very narrow energy intervals. That is, the dose channels are high energy proton detectors with ΔE intervals of only a few MeV for all four domes (except in the inner radiation belt where energy spectra are extremely flat).

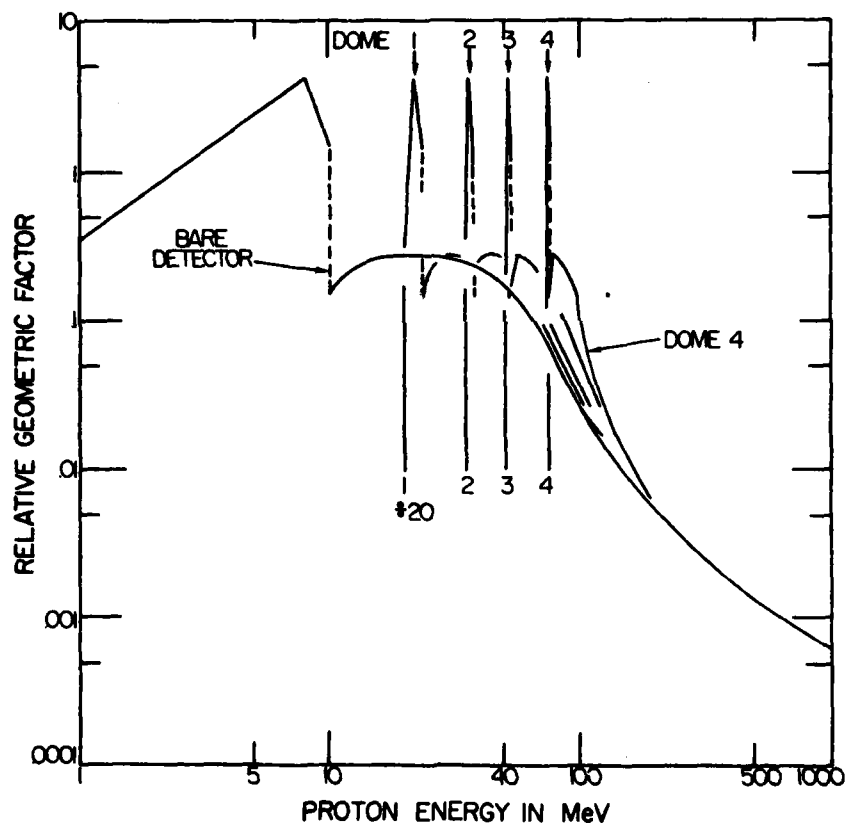


Figure 12. The Response Function of a 400μ Silicon Detector to a Flat Proton Spectrum Which Has a Trapped Mirror Plane Distribution at a Magnetic Inclination Angle of 40° , for Incident Energies Between 1 to 1000 MeV and for Energy Deposition of 1 to 10 MeV (first curve), and Response Functions to the Same Spectrum for the Detector Behind Domes 1, 2, 3, and 4. These response functions apply to the HILET dose channels

The variation of the response function with magnetic inclination shown in Table 7 must be accounted for in deriving proton fluxes and assessing the impact of trapped protons on integrated doses delivered to planar materials such as electronic devices. For much of the inner zone at the DMSP orbit and the currently (1984) observed flat spectrum, this dip angle dependence disappears for the HILET dose channel and count rates may be converted to flux by dividing by a single geometric factor to an accuracy of approximately 50 percent.

The energy independent geometric factors are listed in Table 8 for values of N between 0 and 3.0, and for every 10° magnetic inclination, and for the proton flux and dose channels only. Again, the factors are for an omnidirectional flux confined entirely to the mirror plane. After determining the magnetic inclination of the data set, one determines the value of $j(20)$ in $\text{p/cm}^2 \text{ s MeV}$ in the same way as described above for the isotropic case.

6. ELECTRON RESPONSE FUNCTIONS FROM CALIBRATION DATA

The four LOLET channels, Domes 1 through 4, were calibrated for electron response using the 20 MeV Rome Air Development Center (RADC) electron linear accelerator at Hanscom AFB, Massachusetts. Responses were measured from a few MeV up to 20 MeV. Direct calibration is essential since the large amount of scattering which electrons undergo in the dome shields makes direct response calculation difficult. The data form two sets, one for the total (omnidirectional) geometric factor as a function of energy, and one for the angular response of effective detection area at a fixed electron energy. It was found that all four domes can be fit by a single functional form when the electron energy is normalized to the nominal range-energy threshold of each dome (1, 2.5, 5, 10 MeV, as listed in Table 3).

Table 8. Omnidirectional Geometric Factors for the Trapped Mirror Plane Geometry for HILET Flux (PF) and Dose (PD) Channels in cm² MeV

Magnetic Inclination	PF1	PF2	PF3	PF4	PD1 multiply by 10 ⁻³	PD2 10 ⁻³	PD3 10 ⁻³	PD4 10 ⁻³
N=0								
00.0	1.950	35.59	31.38	28.64	92.20	102.3	341.1	309.5
10.0	1.973	36.05	31.79	29.04	93.04	103.4	345.0	313.3
20.0	2.041	37.48	33.09	30.28	95.35	106.9	356.6	325.7
30.0	2.161	40.05	35.33	32.49	99.12	112.9	373.3	347.4
40.0	2.362	44.01	39.14	35.95	106.7	122.1	410.8	379.9
50.0	2.655	49.83	44.79	40.89	117.2	135.0	465.8	419.5
60.0	3.074	58.28	53.01	48.70	131.7	153.7	545.0	496.5
70.0	3.621	69.17	63.86	58.71	151.0	178.9	649.8	595.0
80.0	3.269	62.63	58.98	54.22	139.9	167.7	625.0	576.5
N=0.5								
00.0	1.587	27.61	22.68	18.56	78.81	83.93	258.2	207.4
10.0	1.603	27.93	22.95	18.81	79.42	84.73	260.8	209.8
20.0	1.651	28.91	23.79	19.56	80.99	87.14	268.1	217.5
30.0	1.733	30.61	25.17	20.88	83.34	91.22	277.0	230.7
40.0	1.865	33.11	27.55	22.89	88.45	97.07	301.1	249.7
50.0	2.040	36.49	30.86	25.56	94.72	104.4	334.3	269.5
60.0	2.251	40.75	35.13	29.51	101.6	113.2	376.3	310.0
70.0	2.415	44.13	38.89	32.95	106.2	120.4	413.0	345.8
80.0	1.968	36.42	32.97	28.35	86.27	99.90	357.2	306.3
N=1.0								
00.0	1.385	23.05	17.52	12.67	71.38	73.43	208.2	145.7
10.0	1.398	23.29	17.70	12.83	71.86	74.04	209.9	147.3
20.0	1.434	23.99	18.26	13.30	73.00	75.85	214.7	152.4
30.0	1.492	25.18	19.15	14.13	74.53	78.77	218.9	160.9
40.0	1.584	26.84	20.71	15.35	78.20	82.68	235.4	172.5
50.0	1.339	28.84	22.72	16.85	82.01	86.78	256.3	182.3
60.0	1.791	30.81	24.97	18.93	84.64	90.40	278.7	204.5
70.0	1.792	31.21	25.88	19.93	82.65	89.52	286.1	215.6
80.0	1.337	23.68	20.34	16.13	59.99	66.53	224.3	176.9
N=1.5								
00.0	1.260	20.15	14.11	8.93	66.79	66.77	174.5	105.5
10.0	1.271	20.33	14.24	9.04	67.18	67.25	175.7	106.6
20.0	1.299	20.85	14.63	9.35	68.05	68.64	178.9	110.0
30.0	1.342	21.71	15.20	9.88	69.04	70.80	180.2	115.5
40.0	1.407	22.82	16.25	10.64	71.77	73.22	191.8	122.8
50.0	1.471	23.98	17.50	11.49	74.01	75.57	205.2	127.4
60.0	1.508	24.83	18.63	12.62	74.16	76.14	216.6	139.9
70.0	1.434	23.80	18.36	12.72	68.87	71.44	210.7	141.2
80.0	0.995	16.76	13.51	9.79	45.57	48.17	151.3	108.7

Table 8. Omnidirectional Geometric Factors for the Trapped Mirror Plane Geometry for HILET (Flux (PF) and Dose (PD) Channels in $\text{cm}^2 \text{ MeV}$ (Contd)

Magnetic Inclination	PF1	PF2	PF3	PF4	PD1 multiply by 10^{-3}	PD2 10^{-3}	PD3 10^{-3}	PD4 10^{-3}
N=2.0								
00.0	1.176	18.14	11.70	6.43	63.69	62.16	150.1	77.81
10.0	1.185	18.28	11.79	6.50	64.02	62.56	151.0	78.55
20.0	1.207	18.68	12.06	6.71	64.70	63.66	153.0	80.86
30.0	1.239	19.30	12.41	7.06	65.32	65.29	152.3	84.61
40.0	1.286	20.05	13.13	7.54	67.41	67.08	160.5	89.26
50.0	1.322	20.66	13.89	8.02	68.58	67.86	169.3	90.94
60.0	1.320	20.78	14.40	8.63	67.15	66.57	174.1	98.05
70.0	1.210	19.16	13.64	8.41	60.12	59.93	162.0	95.63
80.0	0.790	12.60	9.46	6.21	36.86	37.04	107.4	69.69
N=2.5								
00.0	1.116	16.67	9.89	4.70	61.48	58.80	131.5	58.87
10.0	1.124	16.78	9.96	4.74	61.77	59.12	132.1	58.59
20.0	1.142	17.09	10.14	4.88	62.31	60.02	133.2	60.23
30.0	1.166	17.54	10.35	5.12	62.65	61.24	131.2	62.77
40.0	1.199	18.02	10.83	5.42	64.25	62.40	137.1	65.74
50.0	1.215	18.27	11.29	5.69	64.67	62.28	142.7	65.90
60.0	1.188	17.95	11.43	6.01	62.21	59.80	143.6	69.88
70.0	1.061	16.07	10.48	5.71	54.21	52.13	128.6	66.21
80.0	0.657	9.91	6.87	4.06	31.17	29.77	79.02	46.02
N=3.0								
00.0	1.071	15.55	8.50	3.46	59.84	56.23	116.8	43.79
10.0	1.078	15.64	8.54	3.50	60.09	56.49	117.1	44.14
20.0	1.092	15.87	8.67	3.59	60.52	57.23	117.7	45.27
30.0	1.110	16.20	8.76	3.75	60.64	58.15	114.6	46.99
40.0	1.133	16.48	9.09	3.94	61.88	58.85	118.9	48.91
50.0	1.135	16.48	9.35	4.08	61.73	58.08	122.3	48.28
60.0	1.092	15.89	9.27	4.24	58.59	54.82	120.8	50.47
70.0	0.957	13.89	8.27	3.95	50.03	46.58	104.6	46.64
80.0	0.566	8.07	5.13	2.71	27.25	24.74	59.69	30.98

The total geometric factors for an isotropic electron flux, in the LOLET flux channels, are given by the functional forms listed on the following pages by Dome number. In these formulae E_{th} is 1, 2.5, 5, 10 MeV for Domes 1, 2, 3, and 4, respectively. G is in $\text{cm}^2 \text{ sr}$.

$$\begin{aligned}
\text{Dome 1: } G(E/E_{th}) &= 0 & \text{for } E/E_{th} < 1, \\
&= 0.675 (1 - E_{th}/E) & \text{for } 1 \leq E/E_{th} \leq 3, \\
&= 0.45 & \text{for } E/E_{th} > 3.
\end{aligned} \tag{13}$$

$$\begin{aligned}
\text{Domes 2, 3, 4: } G(E/E_{th}) &= 0 & \text{for } E/E_{th} < 1, \\
&= 6.975 (1 - E_{th}/E) & \text{for } 1 \leq E/E_{th} \leq 3, \\
&= 4.65 & \text{for } E/E_{th} > 3.
\end{aligned} \tag{14}$$

The energy dependent geometric factors in Eqs. (13) and (14) are plotted in Figure 13, as well as experimentally determined values. The data are fit well by the functional fits, with the only deviations being at electron energies near threshold where background is a large, uncertain correction, and at 20 MeV where narrow beam characteristics make the monitor detector normalization uncertain (points in brackets). The geometric factors in Eqs. (13) and (14) are useful for near isotropic electron fluxes, and can be used to calculate electron spectra by suitable fitting of the four LOLET flux channel responses for assumed spectral shape, as done for the protons. In particular, if one assumes an isotropic power law spectrum for the electrons of the form:

$$j(E) = j(1) (E_0/E)^N, \tag{15}$$

where $j(1)$ is the differential flux at 1 MeV and $E_0 = 1$ MeV, then, as in Eq. (11), we can define the energy independent geometric factor, $G(N)$:

$$G(N) = \int_E G(E) \{1/E\}^N dE = CR/j(1). \tag{16}$$

Using the definitions of $G(E)$ in Eqs. (13) and (14) and integrating from the threshold energy of a given channel to infinity, we can write an analytic expression for $G(N)$.

$$G(N) = \frac{G_0 \left\{ 1 - 1/3^N \right\}}{E_{th}^{N-1} (N-1) N}. \tag{17}$$

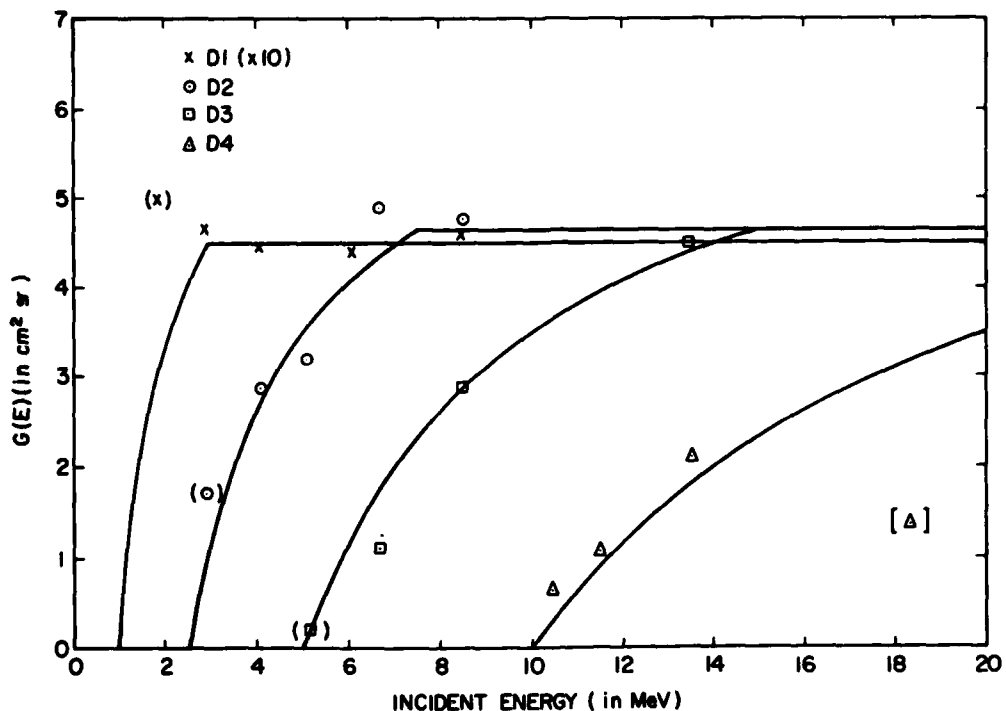


Figure 13. Energy Dependent Geometric Factors as a Function of Energy for Electrons in the LOLET Channels. Points (solid lines) are calibration (fitted) values

In Eq. (17), $G_0 = 0.675 \text{ cm}^2 \text{ sr}$ for Dome 1 and $6.975 \text{ cm}^2 \text{ sr}$ for Domes 2, 3, and 4.

The detailed angular response of the LOLET flux channels for electrons can be fit by an effective area as a function of angle θ relative to the outward view direction of the domes (normal to the detector plane). The effective area, $A(\theta)$ in cm^2 , is:

$$\begin{aligned}
 A(\theta) &= A_0(E) \{2 + 3 \cos \theta\} / 5 & \text{for } 0 \leq \theta \leq 131.8^\circ, \\
 &= 0 & \text{for } \theta > 131.8^\circ.
 \end{aligned} \tag{18}$$

Here,

$$A_0(E) = 0.191 G(E/E_{th}), \tag{19}$$

and $G(E)$ is taken from Eqs. (13) or (14) as appropriate. Comparisons of the fits and data are given in Figure 14 for Dome 2. The fits agree well with the data, particularly considering the uncertain background corrections at energies near threshold. The angular responses of Eqs. (15) and (16) allow the direct calculation of electron spectra for non-isotropic flux distributions.

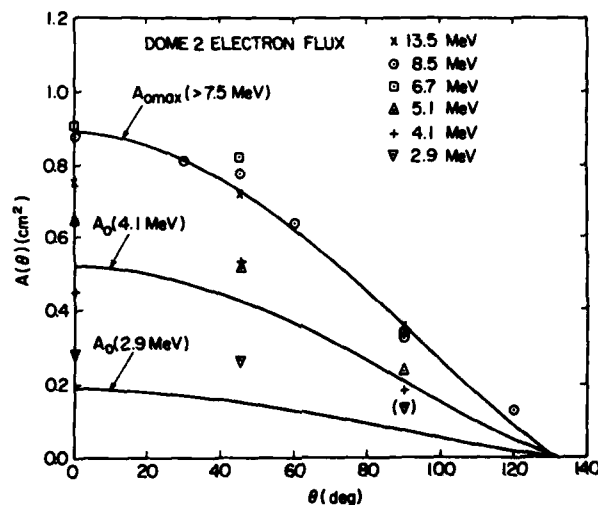


Figure 14. Angular Response to Electrons for the Dome 2 LOLET Channel

It should be noted that in the presence of significant proton fluxes the LOLET fluxes may require correction for the high energy proton contribution. Electron flux angular distributions may require some corrections, but the angular response is relatively flat (compared to protons) so that a first order assumption of isotropic fluxes may be sufficient in most cases. The corrections can then be made by inverting the procedure described in the previous section for determining isotropic proton fluxes, only in this case, knowing $J(20)$ and N one can use the LOLET response functions in Table 4a and Table 4b to find the count rate that will appear in the LOLET channels from protons. Corrections for bremsstrahlung, which are particularly important in the LOLET channels 3 and 4, are discussed in Appendix A.

7. THE STAR COUNTS

'Star counts' as defined in this document refers to counts of very high energy loss events in each of the detectors. The 'star' description comes from the array of emulsion tracks observed when a high energy proton interacts with a nucleus producing secondaries and a recoiling fragment. To be measured as star counts by the dosimeter, minimum energies of 40 MeV for channels 1, 2, and 4, and 75 MeV for channel 3 must be deposited in the detector. This can be accomplished in one of four ways: directly by energy deposition from a high-Z particle (cosmic ray, for example) traversing the detector; indirectly by a high energy proton interacting with a nucleus within the detector; indirectly by a high energy proton interacting with a nucleus outside the detector and a high energy nuclear fragment or secondary depositing the energy in the detector; or directly (in channels 2 and 4 only) by a proton depositing the threshold energy over a long path length. On DMSP, the majority of counts come from protons in the SAA. During large solar flares in the polar regions, solar protons and cosmic ray particles can also produce high level count rates. Separation of the star counts according to sources is non-trivial, but can be attempted under certain circumstances by detailed analysis of the detector response without making the infinite slab approximation, or by modelling the detector response with particle simulation codes using proton flux spectra obtained from the HILET channels.

Star counts are important because they are produced by the same mechanisms that produce single event upsets (SEUs) in microelectronic components. In devices these energy deposits can alter the charge storage state of a device and therefore change the logic configuration producing a bit error. Bit errors can result in erroneous data processing and in extreme conditions they can produce erroneous commands. A short discussion of these effects can be found in Petersen.¹⁴

14. Petersen, E. (1981) Soft errors due to protons in the radiation belt, IEEE Trans. Nuclear Sci., NS-28:3981.

References

1. Hardy, D.A., Schmitt, L.K., Gussenhoven, M.S., Marshall, F.J., Yeh, H.C., Schumaker, T.L., Huber, A., and Pantazis, J. (1984) Precipitating Electron and Ion Detectors (SSJ/4) for the Block 5D/Flights 6-10 DMSP Satellites: Calibration and Data Presentation, AFGL-TR-84-0317, AD A157080, Air Force Geophysics Laboratory, Hanscom AFB, Massachusetts.
2. Smiddy, M., Sagalyn, R.C., Sullivan, W.P., Wildman, P.J.L., Anderson, P., and Rich, F. (1978) The Topside Ionosphere Plasma Monitor (SSIE) for the Block 5D/Flight 2 DMSP Satellite, AFGL-TR-78-0071, AD A058503, Air Force Geophysics Laboratory, Hanscom AFB, Massachusetts.
3. Rich, F.J. (1984) Fluxgate Magnetometer (SSM) for the Defense Meteorological Satellite Program (DMSP) Block 5D-2, Flight 7, AFGL-TR-84-0225, AD A155229, Air Force Geophysics Laboratory, Hanscom AFB, Massachusetts.
4. Gussenhoven, M.S., Hardy, D.A., Rich, F., Burke, W.J., and Yeh, H.-C. (1985) High-level spacecraft charging in the low-altitude polar auroral environment, J. Geophys. Res., 90:11009.
5. Mozer, F.S., Elliott, D.D., Mihalov, J.D., Paulikas, G.A., Vampola, A.L., and Freden, S.C. (1963) Preliminary analysis of the fluxes and spectrums of trapped particles after the nuclear test of 9 July 1962, J. Geophys. Res., 68:641.
6. Paulikas, G.A., and Freden, S.C. (1964) Precipitation of energetic electrons into the atmosphere, J. Geophys. Res., 69:1239.
7. Gary, S.A., and Cashion, R.E. (1971) Solar Proton Monitor for TIROS-M and ITOA Spacecraft, COM-73-10138.
8. Grubb, R.N. (1975) The SMS/GOES Space Environment Monitor Subsystem, NOAA-TM-ERL-SEL-42.
9. Pruett, R.G. (1980) Comparison of DMSP and NTS-2 dosimeter measurements with predictions, J. Spacecraft, 17:270.
10. Sellers, B., Kelliher, R., Hanser, F.A., and Morel, P.R. (1981) Design, Fabrication, Calibration, Testing and Satellite Integration of a Space-Radiation Dosimeter, AFGL-TR-81-0354, AD A113085, Air Force Geophysics Laboratory, Hanscom AFB, Massachusetts.

References

11. Filz, R. C., and Holeman, E. (1965) Time and altitude dependence of 55 MeV trapped protons, August 1961 to June 1964, J. Geophys. Res., 70:5807.
12. Freden, S. C., and Paulikas, G. A. (1964) Trapped protons at low altitudes in the South Atlantic Magnetic Anomaly, J. Geophys. Res., 69:1259.
13. Bischel, H., and Tschalaer, C. (1967) A range-energy table for heavy particles in silicon, Nuclear Data, Section A, 3:343.
14. Petersen, E. (1981) Soft errors due to protons in the radiation belt, IEEE Trans. Nuclear Sci., NS-28:3981.
- A1. Evans, R. D. (1955) The Atomic Nucleus, McGraw-Hill, New York.
- A2. Berger, M. J., and Seltzer, S. M. (1964) Tables of Energy Losses and Ranges of Electrons and Positrons, NASA SP-3012.

Appendix A

Dosimeter Response to Electron Bremsstrahlung

Electrons below 1 MeV can produce a response in all four detectors through the bremsstrahlung they produce. Detailed calculation of the response is difficult because of the complexity of the bremsstrahlung process, and the fact that for the bremsstrahlung energies of importance the dominant interaction in Al (the dome material) and in Si (the detector material) is Compton scattering (Evans^{A1}). An estimate of the bremsstrahlung response can be calculated from the response to an isotropic flux, $J(E_0)$ in $(\text{cm}^2 \text{ s})^{-1}$, of monoenergetic electrons of energy E_0 . The photon spectrum resulting from a single electron of energy E_0 , stopping in the dome material (Al) is assumed to be isotropic, and is written as $d\theta/dE_g$ in photons/electron keV, where E_g is the bremsstrahlung energy. If T_{Al} is the transmission of the bremsstrahlung of energy E_g through the aluminum dome, and $(1 - T_{Si})$ is the effective fraction of photons of energy E_g which are detected in the silicon detector with an energy loss above the threshold of the detector ($E_{th} = 50$ keV for the LOLET channels), then the count rate in the detector from bremsstrahlung, CR_b , may be written:

$$\begin{aligned} CR_b &= (1/8) \int \int A \sin \theta \cos \theta (d\theta/dE_g) J(E_0) T_{Al} (1 - T_{Si}) d\theta dE_g, \\ &= \int \int I(\theta, E_g) d\theta dE_g. \end{aligned} \quad (A1)$$

A1. Evans, R. D. (1955) The Atomic Nucleus, McGraw-Hill, New York.

In Eq. (A1), A is the area of the detector and θ is the angle between the photon direction and the normal to the detector plane. The limits of integration are from 0 to $\pi/2$ for θ , and from E_{th} to E_0 for E .

Similarly, the detected dose rate (energy loss), DR_b in keV/s, due to bremsstrahlung can be written:

$$DR_b = \int \int I(\theta, E_g) \Delta E' dE_g d\theta, \quad (A2)$$

where $\Delta E'$ is defined below.

The transmission of the bremsstrahlung through the aluminum dome, T_{Al} , may be written in terms of the total cross section for photons and the Compton scattering cross section for photons in aluminum. We define the following terms:

τ' = effective thickness of the dome for calculating T_{Al} .

= τ (dome thickness) - R (range in Al for E_0)/2.

μ_t = total cross section for photons of energy E_g in Al, in cm^2/g .

μ'_t = total cross section for photons of energy E'_g in Al, in cm^2/g .

μ_c = Compton scattering cross section for photons of energy E_g in Al, in cm^2/g , and

E'_g = average energy of Compton scattered photons for photons of initial energy, E_g . $E'_g \simeq (E_g - E_c/2)$, where E_c is the maximum energy of a Compton electron from incident photons of energy E_g .

Then,

$$T_{Al} \simeq \exp(-\mu_t \tau') \{1 - \exp(-\mu_t \tau')\} \{ \exp(-\mu'_t \tau'/2) \} \{ \mu_c / \mu_t \}. \quad (A3)$$

Similarly, an expression for $(1 - T_{Si})$ can be written in terms of similar cross sections defined for silicon. Additionally, we define:

μ_{PE} = photoelectron absorption cross section for photons of energy E_g in Si, cm^2/g .

$\bar{\tau}$ = average thickness of the silicon detector for photons, which, for an isotropic flux, is $\sim 2 \tau_0 = 2 \cdot 400 \mu = 0.1864 \text{ g/cm}^2$, and

F' = effective fraction of Compton electrons in silicon from photons of energy E_g which are detected with an energy greater than the threshold energy. $F' \simeq (E_c - E_{th})/E_c$.

Then,

$$(1 - T_{Si}) \simeq \{1 - \exp(-\mu_t \bar{\tau})\} \{ \mu_{PE} + \mu_c F' \} / \mu_t. \quad (A4)$$

Finally, we write the expression for $\Delta E'$:

$$\Delta E' = \{E_{gl} \mu_{PE} + (E_c + E_{th})_1 \mu_c F'/2\} / \{ \mu_{PE} + \mu_c F' \}. \quad (A5)$$

In Eq. (A5), E_{gl} is the limited value of E_g :

$$E_{gl} = E_g, \text{ for } E_g \leq 300 \text{ keV},$$

$$= 150 \text{ keV for } E_g > 300 \text{ keV}.$$

And, $(E_c + E_{th})_1/2$ is the limited value for Compton energy loss in the silicon detector, and has the same limit as E_{gl} .

The form of Eqs. (A1) and (A2) take approximate account of the many complications in the exact calculation. Compton scattering does not reduce photon intensities, but changes the direction and lowers the energy. This results in photon intensities greater than that calculated from total cross section attenuation, and gives the somewhat complicated first order corrected forms for Eqs. (A3) and (A4). Another complication comes from the thin detector thickness of 400μ , which at the average angle of incident of 60° becomes 800μ of silicon, equal to the range of a 446 keV electron and giving an energy loss (ΔE) of 281 keV for minimum ionizing electrons (roughly > 500 keV). Thus, the higher energy Compton electrons do not lose all of their energy in the silicon detector. This is approximately accounted for by Eq. (A5). The limiting values of E_g and $(E_c + E_{th})/2$ are a result of the detector threshold and an assumed flat energy spectrum for the Compton electrons (an approximation consistent with plots in Evans^{A1}).

The bremsstrahlung flux/electron, $d\theta/dE_g$, depends on both the bremsstrahlung cross section and the stopping power of the aluminum domes. The bremsstrahlung spectrum from an electron of energy E_0 is obtained by integrating over the range of the electron (in aluminum), while multiplying each small energy range by the corresponding thin-target bremsstrahlung spectrum. The thin target bremsstrahlung spectrum is approximately flat in energy ($1/E_g$ in photon number) from the electron energy E_0 on down. The total bremsstrahlung spectrum was calculated for various initial electron energies, E_0 , using the total stopping power and the bremsstrahlung

stopping powers in Berger and Seltzer.^{A2} The bremsstrahlung were assumed to be isotropic, which is a good approximation since $J(E_0)$ is assumed to be isotropic and the electrons undergo a large amount of scattering while losing energy.

Eqs. (A1) and (A2) were calculated numerically for the final integral over E_g , and the geometric factor and average (detected) energy/pulse calculated from

$$G_{\text{omni}} (\text{cm}^2) = CR_b / J(E_0) \quad (\text{A6})$$

$$\overline{\Delta E} (\text{keV}) = DR_b / CR_b. \quad (\text{A7})$$

The results for incident electron energies of 0.2, 0.3, 0.5, and 1.0 MeV for all four domes are given in Table A1. The results show that the electron (LOLET) channels are sensitive to low energy (0.2 to 1.0 MeV) electrons with geometric factors four to five orders of magnitude lower than the direct electron geometric factors.

Table A1. LOLET Channel Responses to Electron Bremsstrahlung

Dome No.	1		2		3		4	
Electron Energy, (MeV)	G_{omni} (cm^2)	$\overline{\Delta E}$ (keV)	G_{omni} (cm^2)	$\overline{\Delta E}$ (keV)	G_{omni} (cm^2)	$\overline{\Delta E}$ (keV)	G_{omni} (cm^2)	$\overline{\Delta E}$ (keV)
0.2	1.26(-7)	68	2.15(-6)	69	1.71(-6)	69	1.10(-6)	71
0.3	2.30(-7)	71	3.98(-6)	72	3.27(-6)	73	2.22(-6)	75
0.5	4.85(-7)	81	8.58(-6)	82	7.29(-6)	85	5.33(-6)	89
1.0	1.21(-6)	96	2.20(-5)	98	1.94(-5)	101	1.52(-5)	107
(-n) = 10^{-n}								

A2. Berger, M. J., and Seltzer, S. M. (1964) Tables of Energy Losses and Ranges of Electrons and Positrons, NASA SP-3012.

Appendix B

The J* Interactive Program, JSINTAP

The interactive program JSINTAP is accessed from the Cyber system by the command:

```
/get, jsintap/un=salvett  
/jsintap
```

It responds with the header

JSTR APPLICATION JOB GENERATOR 34

and goes on to list the available options. The options are as follows:

- Option 0: Terminate program now.
This allows the user to leave the interactive program and return to the Cyber system.
- Option 1: List JSTR data between intervals.
This option creates a listing of JSTR data in a user specified time interval. The listing choices are dose, delta dose, ripple counter, delta dose plus ripple counter. These choices apply only to the way the dose data are displayed. There are no options for flux count channels. The data can be printed on paper or output to a file. There is an editor subroutine which allows the user to change the given time interval. The data is listed in 64-sec blocks of 4-sec accumulation intervals.

- Option 2:** Geographic bin sums of counts, doses, fluxes.
This option creates a job to sum, in a user specified geographic interval, star counts, delta dose of protons or electrons, or flux counts of protons or electrons. The user also specifies the time interval and the size of the grid spacing. Note that the geographic intervals, both latitudinal and longitudinal, must be integral multiples of their respective bin sizes.
- Option 3:** Generate a file of J* data.
The user can generate a binary file of J* data for further analysis. User specifications are the time interval and dose option desired. The dose options are dose, delta dose, ripple counter, and ripple counter plus delta dose. The format of the file is as follows:
- ```

CHARACTERISAT*10
1 READ* ISAT, JYR, JDAY, JSED, SDAT, SDLONG, JALT, X, Y,
X Z, SATH, RMLONG, RMALT, KOUNT
DO 2 J=1, KOUNT
2 READ* ITM(J), ICH(J), ISTAR(J), PFLUX(J), IFFLUX(J),
X IPDELTA(J), IRIPP(J), IEDELTA(J), IRIPE(J)
GO TO 1

```
- Option 4:** Generate survey plots.  
This option is used to create survey plots of flux data. Plots can be on paper or microfiche. For microfiche, the time interval is given in whole days, up to three, per job. For paper, the interval is given in seconds. Please note that a large amount of the J\* data has been processed as microfiche plots and is on file in PHP.
- Option 5:** List non-zero star counts.  
This option lists non-zero star counts in user specified time intervals. The listing can be paper printed, dumped to a file, or both.
- Option 6:** Polar pass averages.  
This option lists, for a sequence of polar passes, sums across each pass of the different data. The sums can be of star counts, flux counts (proton or electron), or delta dose counts (proton or electron). The user specifies the time interval and the minimum latitude. The output can be sent to a paper listing, a disk file, or both.
- Option 7:** Polar plotting.  
This option prints histograms of polar pass data on polar plots. The data can be plotted down to a minimum latitude of 45°, and can consist of star counts, flux counts, or delta dose counts. The plots can be on 12-in. or 30-in. paper, or on microfiche.

**Option 8: Day plots (paper).**

This option creates paper plots of dose or flux data for a given whole day. The data points are constructed from 1-min averages of the raw data. The user specifies the mode (dose or flux), the sensor (proton or electron), the channel (1 - 4), and the day.

After listing the available options, the program asks the user to choose one. It goes on to request batch header information, jobname, user name, password, problem and project numbers, and tape information: tape number, label, name. All options will supply a list of available tape information if necessary. It then asks for more specific information pertaining to the chosen option, such as time intervals and type of data requested. Most options have an editor at the end which will allow the user to correct or change the input.

After all information has been received, the program tells on which file the batch job has been written (usually xx or akl), and exits back to the Cyber system. The user must then route the file, xx or akl, with the statement

ROUTE, AKI, DC=IN, TID=C

Most of these jobs have an overnight turnaround. Microfiche plotting can take several days.

U.S. GOVERNMENT PRINTING OFFICE: 1966-600-800-30004

END

10-86

DTIC